

Doctoral Dissertation

博士論文

Transition from Dirac-node semimetal
to magnetic insulator

in perovskite-related iridium oxides

(ペロブスカイト関連イリジウム酸化物における
ディラックノード半金属から磁性絶縁体への転移)

A Dissertation Submitted

for the Degree of Doctor of Philosophy

December 2020

令和2年12月博士(理学)申請

Department of Physics, Graduate School of Science,

The University of Tokyo

東京大学大学院理学系研究科物理学専攻

Masamichi Negishi

根岸 真通

Abstract

Dirac nodes in energy band dispersion of electrons in condensed matter are one of hot topics in research of solid state physics due to their exotic properties including topological protection of the nodes by symmetry. Since the concept of Dirac nodes stands on band theory, i.e., basically single electron picture, electron correlation effects on Dirac materials are one of the interesting problems and have attracted researchers' attention in these years. To tackle this problem, we focused on iridium oxides, where interplays of spin-orbit coupling, correlation and variety of crystal structures provide mines for exotic quantum phases. Among iridates, orthorhombic perovskite AIrO_3 ($A = \text{Sr}, \text{Ca}$) is known as Dirac line node semimetal with correlation. Especially, effective strength of correlation in perovskite iridate can be controlled by changing Sr or Ca in A site. Recently, it is discovered that partial substitution of Ir sites by Sn ions in perovskite SrIrO_3 enhances correlation and triggers a transition from the Dirac semimetal to a magnetic insulator. On the other hand, Sn substitution on perovskite CaIrO_3 which initially has stronger correlation than SrIrO_3 will be a curious problem, but had not been investigated before our work. Therefore, we introduced correlation and disorders by Sn doping in both SrIrO_3 and CaIrO_3 , and compared their responses. By doing that, we tried to investigate effects of underlying correlation in the initial Dirac nodal semimetallic states.

In order to realize the orthorhombic perovskite SrIrO_3 and CaIrO_3 , both metastable at ambient condition, we grew epitaxial thin films of them on perovskite $\text{SrTiO}_3(001)$ substrates. Evaluation of crystal structures using X-ray diffraction and transmission electron microscope confirmed successful realization of epitaxial thin films of the perovskite phases for both SrIrO_3 and CaIrO_3 , and both undoped and Sn doped systems. Especially for SrIrO_3 films, technique using step-terrace structures on substrate was used to control crystalline orientations in film and to suppress twinning.

Then, we performed electric transport measurements for undoped systems in order to check their semimetallic states. Both SrIrO_3 and CaIrO_3 showed almost temperature-independent resistivity, which is consistent with semimetallic electronic states. Perovskite SrIrO_3 film showed negative Hall effect reflecting existence of Dirac electrons as already reported in bulk and films. Our orientation-controlled film helped us to find a characteristic anisotropy of magnetoresistance, though interpretation for it has not been established. Perovskite CaIrO_3 film showed positive Hall effect different from Dirac electron carriers in bulk, which suggests epitaxial strain effect making upper shift of the Dirac node across the Fermi energy.

Next, we compared Sn doped effects on two Dirac semimetals, perovskite SrIrO_3 with weaker correlation and CaIrO_3 with stronger correlation. We found

that they both reach magnetic insulator phases but driving forces of these transitions are contrasting. Sn-doped SrIrO_3 remains semimetallic resistivity against introduction of disorders, and the weak ferromagnetism triggers a transition from semimetal to insulator, similarly to the previous studies on bulk. On the other hand, we discovered that Sn-doped CaIrO_3 develops insulating behavior independently from magnetism. This insulating behavior is probably assisted by both correlation and disorders, suggesting an interplay of correlation and disorders. This discovery of contrasting Sn substitution effects on Sr/CaIrO_3 is the first example to show that different strengths of correlation result in a variety of quantum phases in $5d$ Dirac electron systems.

We also performed detailed characterization of the weak ferromagnetism in Sn-doped perovskite SrIrO_3 . By performing magnetic diffraction using resonant X-ray diffraction, we confirmed that the weak ferromagnetism comes from canting of antiferromagnetic order of Ir moments. We investigated anisotropy of the weak ferromagnetism using the orientation-controlled sample, and discussed the magnetic ordering patterns consistent with the experimental results.

In conclusion, we revealed that perovskite SrIrO_3 and CaIrO_3 , Dirac line node semimetals with different scales of correlation, reach magnetic insulators with different origins under Sn doping, due to interplays of correlation and disorders. This contrast clearly demonstrates different effects of underlying correlation in two Dirac semimetals SrIrO_3 and CaIrO_3 . On the other hand, how topological properties of the symmetry-protected Dirac line nodes appear in these materials remains a future problem.

Contents

1	Introduction	5
1.1	Dirac nodes in materials	5
1.2	Electron correlation	7
1.3	Correlation effects in Dirac materials	7
1.3.1	Example 1: twisted bilayer graphene	8
1.3.2	Example 2: magnetic Weyl semimetals	8
1.4	Correlated Dirac node semimetals perovskite-type iridium oxides	9
1.4.1	Reasons why we focused on perovskite-related iridium oxides	9
1.4.2	Electronic states of iridium oxides	9
1.4.3	Crystal structure of perovskite-type iridium oxides	10
1.4.4	Dirac line nodes	10
1.4.5	Realization of perovskite-type iridium oxides	11
1.4.6	Different correlation in SrIrO_3 and CaIrO_3	11
1.4.7	Review of the previous studies on SrIrO_3	15
1.4.8	Review of the previous studies on CaIrO_3	15
1.4.9	Sn substitution on SrIrO_3	16
1.5	Outline of our study	17
1.5.1	Problems in our study	17
1.5.2	Contents of our study	18
2	Methods	19
2.1	Preparation of thin film samples	19
2.2	Evaluation of samples	20
2.2.1	Stoichiometry	20
2.2.2	X-ray diffraction and X-ray reflectivity	21
2.2.3	Transmission electron microscope	22
2.3	Measurement of electric transport properties	22
2.3.1	Electric resistivity	23
2.3.2	Hall effect	23
2.4	Measurement of magnetism	25
2.4.1	Magnetization	25
2.4.2	Magnetic diffraction using resonant X-ray scattering	26
3	Results and Discussion	29
3.1	Structural evaluation	29
3.1.1	Stoichiometry	29
3.1.2	Orthorhombic perovskite SrIrO_3	29
3.1.3	Orthorhombic perovskite CaIrO_3	33

3.1.4	Discussion	36
3.2	Semimetallic properties of undoped systems	38
3.2.1	Orthorhombic perovskite SrIrO_3	38
3.2.2	Orthorhombic perovskite CaIrO_3	39
3.2.3	Discussion	41
3.3	Sn substitution effects: introduction of correlation / disorders . .	44
3.3.1	Orthorhombic perovskite $\text{SrIr}_{1-x}\text{Sn}_x\text{O}_3$	44
3.3.2	Orthorhombic perovskite CaIrO_3	48
3.3.3	Discussion	56
3.4	Magnetism of Sn-doped perovskite iridates	57
3.4.1	Antiferromagnetism of Ir pseudo-spins	57
3.4.2	Magnetic anisotropy	57
3.4.3	Discussion	59
4	Conclusion	61
5	Acknowledgements	63
A	Monoclinic SrIrO_3	67
A.1	Introduction	67
A.2	Methods	68
A.3	Results	68
A.3.1	Crystal structure	68
A.3.2	Semimetallic properties	69
A.4	Discussion	70
A.4.1	Crystal structure	70
A.4.2	Semimetallic properties	73
B	Data for Hall effect of Sn doped CaIrO_3	74

Chapter 1

Introduction

1.1 Dirac nodes in materials

Dirac equation

$$\left(i\hbar \sum_{\mu=0}^3 \gamma_{\mu} \frac{\partial}{\partial x_{\mu}} - mc \right) \psi = 0 \quad (1.1)$$

is the relativistic equation of motion of a fermion with spin 1/2. Therefore the Dirac equation describes motion of an electron traveling in vacuum with high velocity comparable to light speed.

On the other hand, motion of an electron traveling through materials is affected by periodic potential from lattice. Electronic states inside crystals are usually discussed by energy band theory under one-electron approximation. For some materials with specific band dispersion, motion of a carrier obeys the same equation to the Dirac equation in low energy limit, even though the velocity of the carrier is not at all high as light. Such a class of materials are called Dirac electron systems, or Dirac semimetals¹, and intensively investigated by researchers.

Energy dispersion of a relativistic particle is given like

$$E_{\pm}(\mathbf{k}) = \pm c \sqrt{m^2 c^2 + p^2} = \pm \sqrt{(mc^2)^2 + (\hbar k)^2} = \pm \sqrt{\Delta^2 + v_0^2 k^2}. \quad (1.2)$$

where E_- indicates the negative energy solution of the Dirac equation. Especially, by taking the massless limit $m \rightarrow 0$, Equation 1.2 gives a point node with linear dispersion (Fig. 1.1);

$$E_{\pm}(\mathbf{k}) = \pm |v_0| |\mathbf{k}|. \quad (1.3)$$

Therefore, nodal structures with linear energy dispersion are sometimes called Dirac nodes.

How are Dirac nodes realized in crystals?

Crystals usually have two or more orbits of electrons in a unit cell, and therefore two or more energy levels coexist in the reciprocal space. They will sometimes cross with each other, and, if band crossing occurs, the node formed

¹We used the word “semimetals” to refer to metals whose carriers have smaller Fermi surfaces than usual metals.

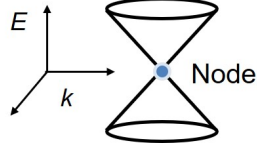


Figure 1.1: Schematic picture of Dirac cone, or the energy-wavenumber dispersion of a massless ($m \rightarrow 0$) Dirac particle.

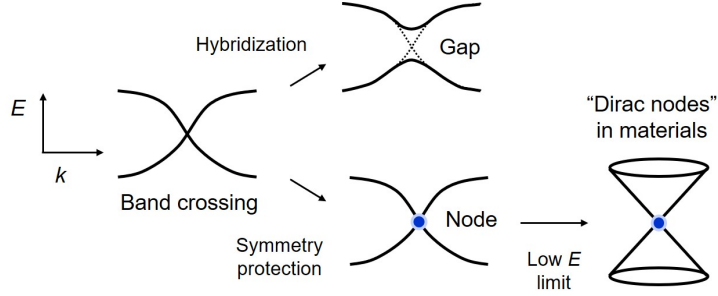


Figure 1.2: Illustration for crossing of energy bands in a material. In case a certain symmetry prevents the crossing point from gap generation due to hybridization of the bands, the nodal structure appears in the material.

by the crossing will often (but not always) have linear dispersion around it. However, such nodes usually form gaps due to hybridization of the concerned orbits. In order to prevent nodes from gap generation, protection by some symmetry is required (Fig. 1.2). Conditions with and without the symmetry protecting the node, which are topologically different situations, will result in clearly different electronic states. Therefore, Dirac nodes in materials are a typical topic of topological materials science. In real materials, Dirac nodes often appear at high symmetry points in reciprocal space due to necessity of symmetry protection.

There are some variations of Dirac nodes.

Focusing on its dimension, the shape of the node can be classified into zero-dimensional, one-dimensional, or two-dimensional. When a node has zero-dimensional shape, it is the point node, often just called a “node.” When one-dimensional, it is line- or curve-shaped, called a “line node” including curving ones. As mentioned later, perovskite SrIrO_3 investigated in this research is predicted to have a ring-shaped Dirac line node. Two-dimensional nodes, called “nodal surfaces”, are theoretically discussed [1, 2], but, to our knowledge, have not been confirmed in real compounds at the moment.

Since Dirac node (Eq. 1.3) is doubly degenerate due to the spin degree of freedom, further splitting of Dirac nodes by symmetry breaking is possible. Split Dirac nodes are called Weyl nodes. Weyl nodes are also found in real materials, and exotic phenomena caused by chiral anomaly are a subject of extensive investigation [3].

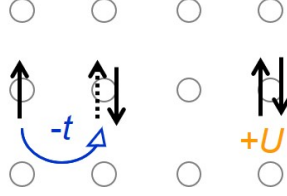


Figure 1.3: Schematic picture for the situation described the Hubbard Model Eq. 1.4. Gray circles: sites which can contain one electron with up spin and one electron with down spin for each. Black solid arrows: electrons with spin directions. Black dashed arrow: no electron at the site with the given spin direction.

1.2 Electron correlation

Electron correlation refers to electron-electron interactions in materials. Electron correlation is the source of many important phenomena in solid state physics, such as magnetism, or Mott transition, etc. Because of the difficulty of many body quantum problems, correlation effects in materials remain one of the hot topics in research of condensed matter physics.

The Hubbard model is a simple model to describe electron correlation. The Hubbard model considers correlation as on-site Coulomb repulsion. Considering the situation where electrons can move to nearest neighbor sites (Fig. 1.3), the Hamiltonian for Hubbard model is given as

$$H = -t \sum_{(i,j),\sigma} (c_{i\sigma}^\dagger c_{j\sigma} + c_{j\sigma}^\dagger c_{i\sigma}) + U \sum_i n_{i\uparrow} n_{i\downarrow}. \quad (1.4)$$

The first term of Eq. 1.4 describes hopping of electrons to nearest neighbor sites, and t indicates the transfer energy of the hopping. The Hamiltonian containing only the first term corresponds to a single electron picture treated in usual band theory, and t is proportional to the width of the energy band. The second term describes on-site Coulomb repulsion, and U indicates the Coulomb energy in case two electrons exist in the same sites.

According to this Hubbard model, the ratio of the second term against the first term indicates the effective strength of electron correlation in the system. If this ratio is much smaller than one, correlation will have little effects on the system. If this ratio is much larger than one, properties of the system will be governed mainly by correlation. Therefore, cases where transfer and correlation have similar energy scales will be interesting for investigation of correlation effects. One more finding from the Hubbard model is that effective strength of correlation can be modified by changing the transfer term. For example, one can modify the transfer term by changing the transfer energy t or number of hopping bonds, which will be easier than changing the Coulomb repulsion itself.

1.3 Correlation effects in Dirac materials

Because the concept of Dirac nodes stands on energy band picture, i.e., one-electron approximation, the effect of electron correlation on Dirac materials is

not trivial at all, but an interesting problem to tackle. We pick up two examples of novel correlation effects in Dirac materials. The first one is twisted bilayer graphene, and the second one is magnetic Weyl semimetals.

1.3.1 Example 1: twisted bilayer graphene

Graphene is a famous example for two dimensional Dirac semimetal [4]. Single layer graphene hosts Dirac point nodes and massless Dirac fermions. The degeneracy at the Dirac points is protected by symmetry between two triangular sublattices in the honeycomb lattice of graphene.

Graphene can be stacked by van der Waals interaction between the layers. Bilayer graphene contains two single layer graphenes connecting each other. Because the sublattice symmetry is broken in bilayer graphene, the Dirac nodes open gaps, and therefore bilayer graphene hosts massive Dirac fermions. If many layers of graphenes stack, bulk material graphite will be obtained.

In recent years, techniques to stack two dimensional materials like graphene with a given rotational angle have been developed and opened a new field to synthesize van der Waals heterostructures. When two graphenes stack each other with a non-trivial rotational angle, a Moiré pattern appears and a large superlattice is formed. Properties of such twisted bilayer graphene can be modified by changing the stacking angle [5].

Recently, correlation phenomena like superconductivity and Mott-like insulator were discovered and investigated in twisted bilayer graphene with twist angle $\sim 1.1^\circ$ [6, 7].

1.3.2 Example 2: magnetic Weyl semimetals

As already introduced, Weyl nodes refer to spin-split massless Dirac nodes in materials science. Weyl pairs are located in different points in momentum space, and display exotic phenomena like Fermi arcs and chiral anomaly-driven magneto-transport properties [3].

In order to realize Weyl nodes in materials, breaking of inversion and/or time-reversal symmetries is necessary. For example, the first experimentally discovered Weyl semimetal TaAs is categorized into the inversion-symmetry-broken type [3]. Examples for the time-reversal-symmetry-broken type, which results that that material has magnetism, are Mn_3B [8] and $\text{Co}_3\text{Sn}_2\text{S}_2$ [9]. Since magnetism is a typical correlation effect, time-reversal-symmetry-broken Weyl semimetals, or magnetic Weyl semimetals, is one form of correlation effects on Dirac nodes.

One of characteristic features of magnetic Weyl semimetals is anomalous Hall effect. Anomalous Hall effect appears in time-reversal-symmetry-broken, or ferromagnetic, materials. There are several mechanisms which can cause anomalous Hall effect, and one of them implies that non-zero Berry curvature causes anomalous Hall effect [10]. Because magnetic Weyl semimetals are defined by coexistence of magnetism and Weyl nodes and Weyl nodes are sink and source of Berry curvature, magnetic Weyl semimetals sometimes show large anomalous Hall effect.

1.4 Correlated Dirac node semimetals perovskite-type iridium oxides

1.4.1 Reasons why we focused on perovskite-related iridium oxides

Our motivation to research is to explore correlation effects on Dirac materials. To tackle this problem, we focused on iridium oxides (iridates) with perovskite-related structures. We use the word “perovskite-related structures” to refer to “crystal structures which contain octahedral units of IrO_6 , one Ir^{4+} ion is surrounded by six O^{2-} ions, and are constructed by connections of those units.” There are two advantages to choosing this material group to find candidates for correlated Dirac materials.

The first advantage is its variety of crystal structures. The family of perovskite-related materials forms a variety of crystal structures by changing connections between octahedral units IrO_6 , including corner-, edge- and face-sharing connections. Because Ir-O-Ir bonds have an important role in formation of electronic band structure, a wide variety of octahedral connections directly results in a wide spectrum of ground states from metal to insulator. In terms of the Hubbard models, perovskite-related structures realize a variety of the transfer term $-\sum t c^\dagger c$, and therefore a variety of effective strength of correlation. Various crystal symmetries can benefit also for the exploration of topological materials.

The second advantage is electronic states. In iridium oxides with tetravalent iridium ions, the interplay of crystal field splitting and strong spin orbit coupling combines $5d$ orbits and spins into a spin-orbit-entangled state with effective angular momentum $1/2$. Therefore, the materials are regarded as half-filled pseudo-spin $1/2$ systems, a playground to research correlation, magnetism and metal-insulator transition. This mechanism is explained in the following section.

1.4.2 Electronic states of iridium oxides

In many iridium oxides (iridates) including Ir^{4+} ions, one Ir^{4+} ion is surrounded by six O^{2-} ions and they form the octahedral structure. Ir^{4+} ion has the electronic configuration $[\text{Xe}] 4f^{14} 5d^5$. Ir^{4+} ions in oxides have the ground states where orbital angular momentum \mathbf{L} and spin angular momentum \mathbf{S} are combined by the strong spin-orbit coupling.

d orbitals include five-degenerate components, d_{xy} , d_{yz} , d_{zy} , $d_{x^2-y^2}$ and $d_{3z^2-r^2}$. $1/2$ spins include two components, $\pm\sigma$. Thus, d states include ten states. In the octahedral structure, the five d orbitals split to two energy levels, three-degenerate t_{2g} orbits and two-degenerate e_g orbits. The Ir^{4+} ion has five electrons in $5d$ orbits and takes a low spin state due to the large crystal field splitting between t_{2g} and e_g . Therefore, in the ground states, the t_{2g} level has five electrons while the e_g level has no electron. Then, spin orbit coupling $\eta \mathbf{l} \cdot \mathbf{s}$ ($\eta > 0$) splits the t_{2g} states to two energy levels, the lower quartet stabilized by $\eta/2$ and the higher doublet destabilized by η . The former is called as the $j_{\text{eff}} = 3/2$ level and the latter is called as $j_{\text{eff}} = 1/2$ level, from the analogy of splitting of p orbitals with $l = 1$ by spin-orbit coupling. In the ground states, the $j_{\text{eff}} = 3/2$ level has four electrons (full-filled) and the $j_{\text{eff}} = 1/2$ level has one electron (half-filled). As a result, the doubly degenerate ground states with the total effective angular momentum $J_{\text{eff}} = 1/2$ are obtained (Fig. 1.4).

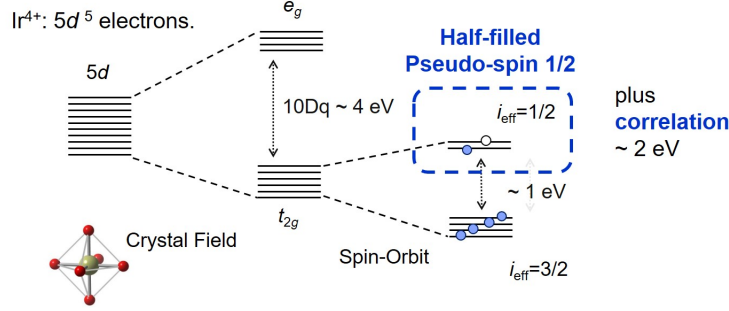


Figure 1.4: Schematic picture of the $J_{\text{eff}} = 1/2$ states.

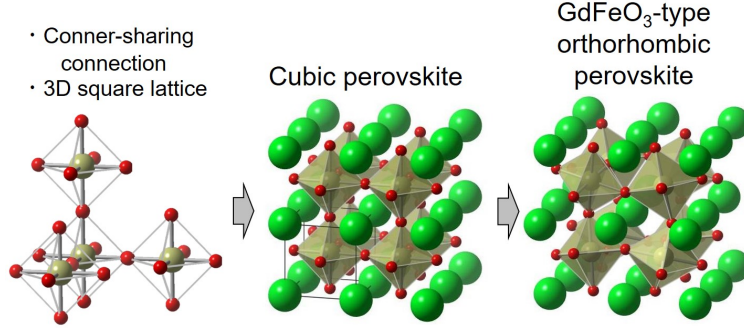


Figure 1.5: Crystal structure of perovskite-type iridates AIrO_3 ($A = \text{Sr}, \text{Ca}$). Lime balls: Sr or Ca. Yellow balls: Ir. Red balls: O.

This $J_{\text{eff}} = 1/2$ picture is confirmed in the monolayer perovskite Sr_2IrO_4 by resonant X-ray scattering measurements [11, 12].

1.4.3 Crystal structure of perovskite-type iridium oxides

Alkaline earth metal iridates AIrO_3 ($A = \text{Sr}, \text{Ca}$) with perovskite-type crystal structures are known as candidates of Dirac line node semimetals [13, 14].

Perovskite-type crystal structure is obtained by a three-dimensional square (cubic) network of IrO_6 octahedra connecting each other at their corners. In AIrO_3 ($A = \text{Sr}, \text{Ca}$), perovskite structures have rotating and tilting distortions of the octahedra, and deform from cubic to orthorhombic, like GdFeO_3 [15, 16] (Fig. 1.5). These GdFeO_3 -type orthorhombic perovskite structures have $\sqrt{2} \times \sqrt{2} \times 2$ times larger unit cells than cubic perovskites, and contain four iridium ions in the unit cell. The space group is No. 62 ($Pbnm$), which is characterized by n -glide, b -glide, and c -mirror symmetries. This crystal symmetry includes nonsymmorphic symmetries (the two glide symmetries), which concerns protection of the line nodes, as explained in the following section.

1.4.4 Dirac line nodes

J.-M. Carter *et al.* (2012) pointed out the ring-shaped nodal line in the energy band dispersion of orthorhombic perovskite SrIrO_3 by performing band calcula-

tions using density functional theory and tight binding model [13]. It is located around the U point on the edge of the Brillouin zone and lies in the UXSR plane (Fig. 1.6). Y.Chen *et al.* (2016) [17] revealed more detailed theoretical analysis on symmetry protection of the line nodes using a tight binding model based on the $J_{\text{eff}} = 1/2$ picture. Since the unit cell contains four iridium sites, there are four $j_{\text{eff}} = 1/2$ bands in the momentum space, where each has the Kramers degeneracy of the $j_{\text{eff}}^z = \pm 1/2$ states. At the U point, the four bands form two degenerating pairs due to the n -glide symmetry of the crystal. On the other hand, on the XS and RS lines, the two pairs exchange their partners for degeneracy due to the n - and b -glide symmetries. Therefore, crossing by two $j_{\text{eff}} = 1/2$ bands occurs in the UXSR plane and a ring-shaped line node is formed around the U point (Fig. 1.7). A gap generation at the node is also forbidden by the glide symmetries. Since the $j_{\text{eff}} = 1/2$ bands are half-filled, the node will be located near the Fermi level.

Because the line node is protected by the time-reversal and crystal symmetry, partial breaking of the symmetries will turn the system topologically different phases. For example, the Dirac line node will turn to Weyl line nodes or Dirac point nodes under an external magnetic field depending on direction of the field [17] (Fig. 1.8). A field along the crystalline a axis will change the Dirac ring to two Dirac point nodes. A field along the b axis will change the Dirac ring to two Weyl rings. A field along the c axis will make a fully gapped state.

Energy band structure of orthorhombic perovskite CaIrO_3 who has the same space symmetry also hosts similar Dirac line nodes. Band calculation on perovskite CaIrO_3 using density functional theory and including correlation effects by dynamical mean field theory supports the existence of the Dirac line node (Fig. 1.9) [14].

1.4.5 Realization of perovskite-type iridium oxides

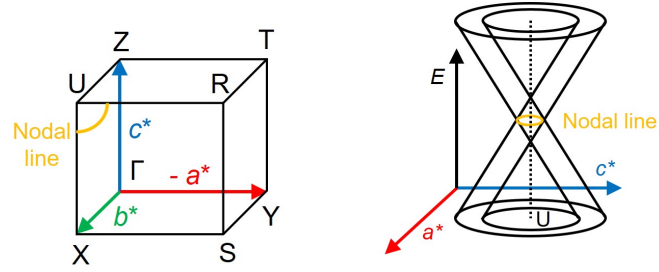
It is already known that both SrIrO_3 and CaIrO_3 realize the GdFeO_3 -type orthorhombic perovskite structures as metastable phases at ambient condition. Fig. 1.10 shows temperature-pressure phase diagrams of bulk SrIrO_3 and CaIrO_3 obtained by the previous studies [15, 18]. According to the phase diagrams, perovskite SrIrO_3 is a high-pressure-favored phase, and perovskite CaIrO_3 is low-pressure-favored but still metastable at ambient pressure and temperature. Therefore, bulk synthesis, especially single crystal growth, has technical difficulties for both SrIrO_3 and CaIrO_3 . Single crystal growth for perovskite CaIrO_3 succeeded just a few years ago [14].

The other approach to obtain the perovskite phases of SrIrO_3 and CaIrO_3 is epitaxial growth on single crystalline substrates with perovskite structures. Epitaxial thin films of perovskite SrIrO_3 have been grown on various substrates [19, 20], and perovskite CaIrO_3 films have also been grown on $\text{GdScO}_3(110)$, $\text{YAlO}_3(110)$, $\text{NdGaO}_3(110)$, $\text{LaAlO}_3(001)$, $\text{SrTiO}_3(001)$, $\text{GdScO}_3(110)$ and $\text{LSAT}(001)$ [21, 22, 23, 24].

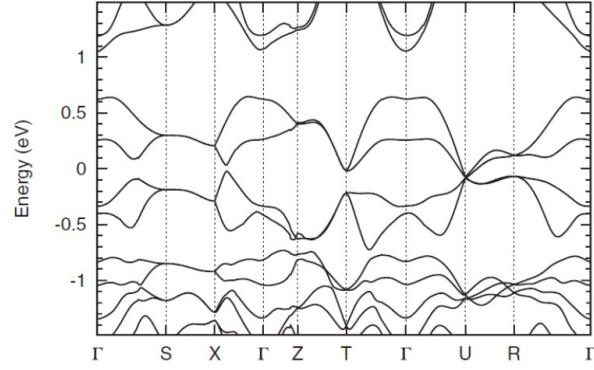
1.4.6 Different correlation in SrIrO_3 and CaIrO_3

Next we discuss the difference between perovskite SrIrO_3 and CaIrO_3 .

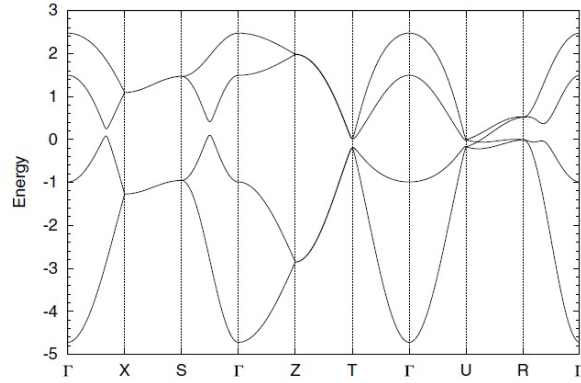
The lattice parameters of perovskite SrIrO_3 are reported as $a = 5.597(1) \text{ \AA}$, $b = 5.581(1) \text{ \AA}$ and $c = 7.752(2) \text{ \AA}$ [25], while those of CaIrO_3 are given as



(a) Brillouin zone and location of the line node. (b) Schematic picture of the ring-shaped line node around the U point.



(c) LDA+U calculation including spin orbit coupling.



(d) Band calculation by tight binding model based on the $J_{\text{eff}} = 1/2$ picture.

Figure 1.6: Band structure of orthorhombic perovskite SrIrO_3 . The figures (c) and (d) are quoted from J.-M. Carter *et al.* (2012) [13].

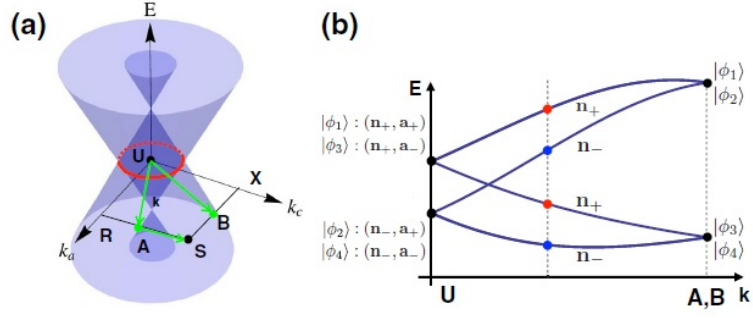


Figure 1.7: Illustration for the Dirac line node in SrIrO_3 . The figures are quoted from Y.Chen *et al.* (2016) [17].

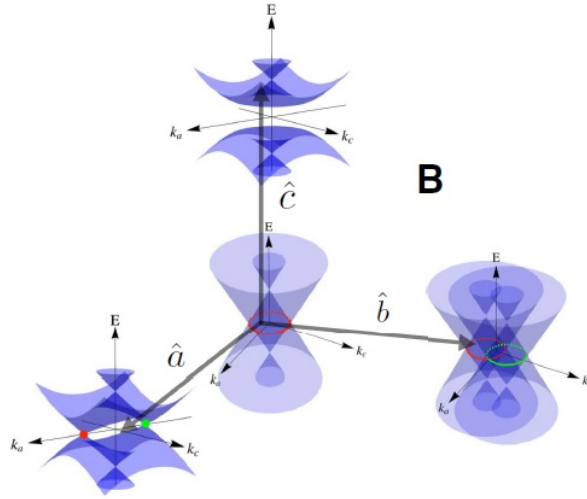


Figure 1.8: Illustration for topological transitions of the Dirac line node in SrIrO_3 by external magnetic fields. The figure is quoted from Y.Chen *et al.* (2016) [17].

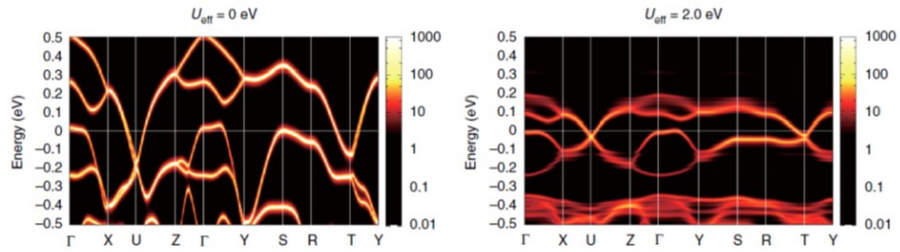


Figure 1.9: Band structures of perovskite CaIrO_3 calculated using density functional theory + dynamical mean field theory. The figures are quoted from J. Fujioka *et al.* (2019) [14].

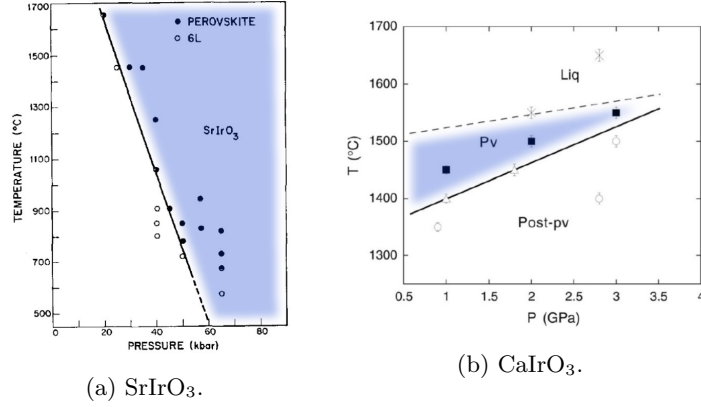


Figure 1.10: Temperature-pressure phase diagrams of SrIrO₃ and CaIrO₃. The blue colored regions are GdFeO₃-type orthorhombic perovskite structures. The figures (a) is quoted from J. M. Longo *et al.* (1971) [15], and the figures (b) is quoted from K. Hirose *et al.* (2005) [18]. The blue colored layers are added by the authors.

Table 1.1: Sn-O-Sn bond angles θ_{ab} and θ_c , and Sn-O bond lengths d_{ab} and d_c of orthorhombic perovskite SrSnO₃ and CaSnO₃ from the crystal structures reported in the previous study [27].

	θ_{ab}	θ_c	d_{ab}	d_c
SrSnO ₃	156.72°	156.23°	2.054 Å	2.060 Å
CaSnO ₃	148.20°	146.66°	2.061 Å	2.063 Å

$a = 5.3597(5)$ Å, $b = 5.6131(4)$ Å and $c = 7.6824(8)$ Å [14]. Therefore, the volume of the unit cell of perovskite CaIrO₃, 231.12 Å^3 , is smaller than that of SrIrO₃, 242.15 Å^3 . This difference is explained by the smaller ionic radius of Ca²⁺, 1.34 Å, than that of Sr²⁺, 1.44 Å [26]. Thus, perovskite CaIrO₃ should have more distortions of IrO₆ octahedra from cubic perovskite in order to realize the smaller unit cell than CaIrO₃. As supporting data, we display in Table 1.1 Sn-O-Sn bond angles and Sn-O bond lengths in SrSnO₃ and CaSnO₃ which both have GdFeO₃-type orthorhombic perovskite structures² [27]. Sn-O bond lengths do not differ so much for SrSnO₃ and CaSnO₃, but Sn-O-Sn bond angles of CaSnO₃ are clearly smaller than those of SrSnO₃.

The more octahedral distortions in CaIrO₃ will make overlapping of orbitals of Ir and O smaller, and will result in smaller transfer energy between Ir sites via O ions. In terms of the Hubbard model Eq. 1.4, this means a smaller t factor. Therefore, the octahedral distortions will reduce total transfer energy, i.e., bandwidth, and then will enhance effective strength of electron correlation. Correlation in CaIrO₃ is estimated to be 20 % larger than that of SrIrO₃ [14].

²We could not find a reliable data set of crystal structures of SrIrO₃ and CaIrO₃. Since both perovskite Sr/CaIrO₃ are metastable, their lattice parameters may depend on preparation methods.

1.4.7 Review of the previous studies on SrIrO₃

Properties of bulk

SrIrO₃ takes a monoclinic phase at ambient pressure. High pressure high temperature synthesis under 4 GPa at 1000°C realizes the orthorhombic perovskite phase, which is metastable at ambient condition. There are a few previous researches on perovskite SrIrO₃ using polycrystalline bulk samples [15, 28, 29, 30].

According to these reports, perovskite SrIrO₃ is paramagnetic [15], and shows semimetallic resistivity which gradually becomes smaller as cooled down [30]. Hall coefficient is negative, and $|R_H|$ becomes smaller as temperature increases. This negative Hall signal is attributed to Dirac electrons [30]. Magnetoresistance shows positive linear component both for $B \parallel I$ and $B \perp I$ cases. This positive MR may be attributed to the linear MR at quantum limit [31], or it may reflect transform of the Dirac node under external field [17, 30].

Properties of thin films

Perovskite SrIrO₃ grows on SrTiO₃(001) substrate with the c axis of the original orthorhombic unit cell parallel to $[100]$ or $[010]_{\text{STO}}$ directions [32]. In such cases where the c axis lies along in-plane directions, epitaxial strain from cubic or orthorhombic substrates deforms the crystal structure of perovskite SrIrO₃, and the $Pbnm$ symmetry changes to $P112_1/m$ [33, 34]. Therefore, in epitaxial thin films, the line node of SrIrO₃ is allowed to have a small gap. The gap size for SrIrO₃ / GdScO₃(110) is estimated as ~ 3 meV [33].

Energy band dispersion of perovskite SrIrO₃ thin films was investigated by angle-resolved photoemission spectroscopy (ARPES) [35, 36]. These studies confirmed the semimetallic state with both electrons and holes. Especially, ARPES observed a small electron pocket at the U point, which is regarded as the Dirac electron band. The Dirac node is located ~ 50 meV below E_F . However, detailed dispersion, especially structure of the Dirac node is still unclear.

Perovskite SrIrO₃ thin film typically shows paramagnetism and semimetallic resistivity [37]. When film thickness is small ($\leq 3 - 4$ nm), the film becomes insulating [38]. This semimetal to insulator transition is attributed to correlation effect enhanced by lower dimensionality. When film thickness is large (170 nm), the crystal structure relaxes [32]. Films thinner than 35 nm do not show the relaxation [38].

Recently, a technique for orientation control of perovskite SrIrO₃ thin films on SrTiO₃(001) substrates using step edges is reported by the other group [39]. In this study, we developed the same technique and applied to the synthesis of perovskite SrIr_{1-x}Sn_xO₃ films.

1.4.8 Review of the previous studies on CaIrO₃

Properties of bulk

Orthorhombic perovskite CaIrO₃ is also metastable. J. Fujioka *et al.* (2018) successfully obtained single crystals of perovskite CaIrO₃ and found that it hosts high mobility (over $60000 \text{ cm}^2\text{V}^{-1}\text{s}^{-1}$) electron carriers [14]. They also succeeded to observe Shubnikov-de Haas (SdH) oscillations from the Fermi surface of the Dirac electron pockets. They propose that strong correlation of CaIrO₃

would help to put the Dirac node near the Fermi level by narrowing the band width, which would result in the appearance of high mobility electrons.

The temperature-dependent resistivity of the bulk CaIrO_3 crystal is characteristic. It stays at almost the same value above 100 K, shows insulator-like divergence in range $20 \text{ K} \lesssim T \lesssim 100 \text{ K}$, and then becomes small below 20 K. This behavior reflects the carrier balance of the semimetallic state. Nonlinear $\rho_{yx}(B_z)$ also indicates coexistence of different carriers.

Pressure effect on the electronic state and the transport properties are also investigated by using pressured single crystals [40]. Pressure-caused changes of Hall resistivity and SdH oscillations revealed that pressure deforms the energy band structure and shifts the nodal level downwards. They estimate that 1 GPa pressure makes the nodal energy level 5 meV lower.

Properties of thin films

Perovskite CaIrO_3 films have been grown on $\text{GdScO}_3(110)$, $\text{YAlO}_3(110)$, $\text{NdGaO}_3(110)$, $\text{LaAlO}_3(001)$, $\text{SrTiO}_3(001)$, $\text{GdScO}_3(110)$ and $\text{LSAT}(001)$ [21, 22, 23].

One significant character of CaIrO_3 films is large substrate-dependence, i.e., epitaxial strain effect, of transport properties. For example, CaIrO_3 films on $\text{SrTiO}_3(001)$ show positive Hall signal at low temperature and signature-flipping of R_H by temperature [23]. These properties are very different from negative R_H of bulk crystals. This drastic strain effect suggests that the Dirac node easily moves across the Fermi level by deformation of band structure.

1.4.9 Sn substitution on SrIrO_3

The previous studies on bulk

The works on Sn-doped perovskite strontium iridate $\text{SrIr}_{1-x}\text{Sn}_x\text{O}_3$ report the appearance of weak ferromagnetic insulator phase [41, 42, 43]. Neutron diffraction detects G -type antiferromagnetic order of Ir pseudo-spins [42]. Thus, the weak ferromagnetism comes from canting of the antiferromagnetic order of Ir pseudo-spins.

Possible effects of partial substitution of Ir by Sn

We discuss possible effects of partial substitution of Ir by Sn in perovskite Sr/CaIrO_3 .

Because totally substituted limits SrSnO_3 and CaSnO_3 also take GdFeO_3 -type orthorhombic perovskite structures like Sr/CaIrO_3 [27], Sn substitution on Sr/CaIrO_3 will ideally trigger no structural transition. Because Ir^{4+} and Sn^{4+} are both tetravalent, substitution will ideally cause no carrier doping effect. Because Sn^{4+} ion is non-magnetic, substitution is not an introduction of magnetic impurities. Then, we propose two possible effects of Sn substitution.

The first one is reduction of transfer, or enhancement of effective strength of correlation. Sn substitution will reduce the number of Ir sites and cut Ir-Ir bonds in the system. In terms of the Hubbard model Eq. 1.4, decrease of Ir sites means reduction of summation for index i for both the first and the second terms, and decrease of averaged number of nearest neighbor Ir sites means reduction of summation for pair of indices (i, j) , or just index j , for only the first transfer term. Therefore, substitution will relatively suppress the first transfer term

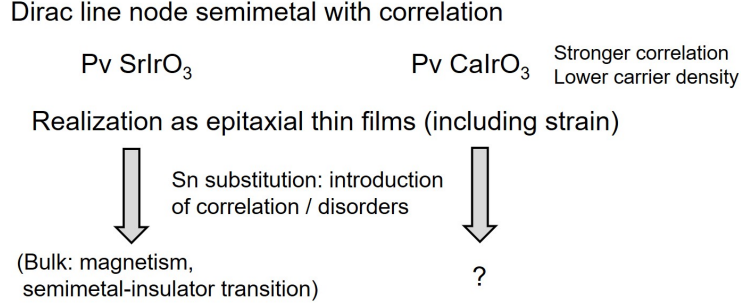


Figure 1.11: Outline of our study.

compared to the second correlation terms. We think that this mechanism may explain the origin of the antiferromagnetic order of Ir pseudo-spins observed in bulk $\text{SrIr}_{1-x}\text{Sn}_x\text{O}_3$.

The other possible effect is an introduction of disorders in the Ir conduction network. It may enhance localization effects of carriers especially at low temperature, but it is still unclear about the roles of disorders in $\text{SrIr}_{1-x}\text{Sn}_x\text{O}_3$.

1.5 Outline of our study

1.5.1 Problems in our study

In this study, we synthesized epitaxial thin films of perovskite SrIrO_3 and CaIrO_3 , and compared Sn substitution effects on them (Fig. 1.11). In this section, we explain physical meanings of our works and problems we tried to approach.

As discussed in the previous sections, perovskite iridates SrIrO_3 and CaIrO_3 are predicted as candidates for Dirac line node semimetals protected by crystal symmetry, and experimental results support the existence of the Dirac nodes in both materials. Electron correlation also has important roles in these iridates, and effective strength of electron correlation can be controlled by switching Sr and Ca. SrIrO_3 is semimetal with Dirac electrons and underlying correlation, and CaIrO_3 has smaller carrier density of Dirac electrons and stronger correlation. These characters of perovskite iridates can be summarized as “Dirac line node semimetals with underlying and controllable electron correlation.”

Sn substitution on such correlated semimetals will enhance correlation and introduce disorders at the same time. The previous studies on bulk $\text{SrIr}_{1-x}\text{Sn}_x\text{O}_3$ revealed that enhanced correlation triggers magnetism, and the magnetism triggers a transition from semimetal to insulator. How about CaIrO_3 which is more close to criticalities of both correlation and energy level of the Dirac node? This question is not at all trivial, but is interesting in terms of possible interplays of correlation, disorders, and topologically protected nodal semimetallic state. In addition, the comparison of Sn doping effects on SrIrO_3 and CaIrO_3 may outline roles of electron correlation underlying in the original Dirac semimetallic states. These two are our main problems in this study.

We take growth of epitaxial thin films to obtain metastable perovskite phases. As a result, it introduces epitaxial strain into the system. Epitaxial strain effects

on correlated Dirac semimetals Sr/CaIrO₃ are also an interesting side problem.

1.5.2 Contents of our study

We synthesized orthorhombic perovskite $\text{Alr}_{1-x}\text{Sn}_x\text{O}_3$ ($A = \text{Sr}$ or Ca , $0 \leq x \leq 0.2$) thin films on $\text{SrTiO}_3(001)$ substrates by pulsed laser deposition. For $\text{SrIr}_{1-x}\text{Sn}_x\text{O}_3$ films, vicinal $\text{SrTiO}_3(\delta 01)$ substrates were used to control crystalline orientation.

The crystal structures of the samples were evaluated by X-ray diffraction, X-ray reflectivity, and observation and electron diffraction using a transmission electron microscope.

The electric transport properties, resistivity and Hall effect, of the samples were measured. For Sn doped samples, magnetization was also measured. Magnetic diffraction of the $\text{SrIr}_{0.8}\text{Sn}_{0.2}\text{O}_3$ film on $\text{SrTiO}_3(001)$ substrates using resonant X-ray scattering at the L_3 edge of iridium was also measured.

The chapter for the experimental results and discussion is divided into four sections;

1. Evaluation of crystal structures of the thin film samples, including results of X-ray diffraction and transmission electron microscope.
2. Electric transport properties of undoped systems.
3. Evaluation of Sn substitution effects, including magnetic properties and electric transport properties.
4. Characterization of magnetic structure of $\text{SrIr}_{0.8}\text{Sn}_{0.2}\text{O}_3$ films, including results of resonant X-ray scattering and magnetic anisotropy.

Appendix contains a short introduction and evaluation of crystal structure and transport properties of monoclinic SrIrO_3 epitaxial thin film, candidate for Dirac semimetal with two distinct nodes.

Chapter 2

Methods

2.1 Preparation of thin film samples

In this research, thin film samples of orthorhombic perovskite $AIr_{1-x}Sn_xO_3$ ($A = \text{Sr or Ca}$, $0 \leq x \leq 0.2$) were prepared by pulsed laser deposition (PLD) method (Fig. 2.1).

We used sintered pellets of $AIr_{1-x}Sn_xO_3$ as PLD targets. For synthesis of the targets, powder of ACO_3 , IrO_2 and SnO_2 was mixed with molecular ratio $1 : 1.05(1 - x) : 1.05x$. ACO_3 powder was heated for 12 hours at 200°C in air before weighing. Then, the mixed powder was pelletized and heated for 8 hours at 800°C in air (Fig. 2.2a). This heating process removes CO_2 from ACO_3 and reduces density of the pellet. Then, the material was again pelletized and heated for 50 hours at $1000\text{--}1100^\circ\text{C}$ in air (Fig. 2.2b). The obtained pellets were used as the targets.

Cubic perovskite strontium titanate $SrTiO_3$ (STO) single crystalline plates with polished (001) surface were used as substrates for crystal growth. For control of crystalline orientation of orthorhombic $AIr_{1-x}Sn_xO_3$ films, vicinal $STO(\delta 01)$ substrates with surface 0.4° -tilted from (001) to $[100]$ direction were used. Vicinal substrates were BHF-etched by the maker and heated for 1 hour at 1050°C in air by the authors to obtain an atomically flat surface with step-

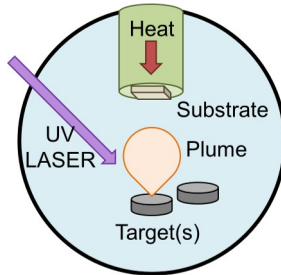


Figure 2.1: Schematic picture of experimental set-up for pulsed laser deposition.

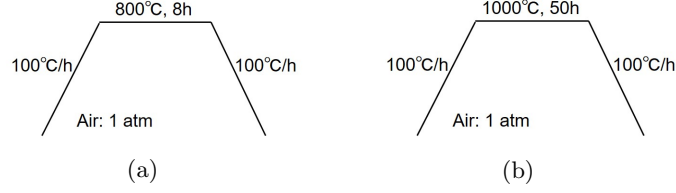


Figure 2.2: Sequences for synthesis of PLD targets.

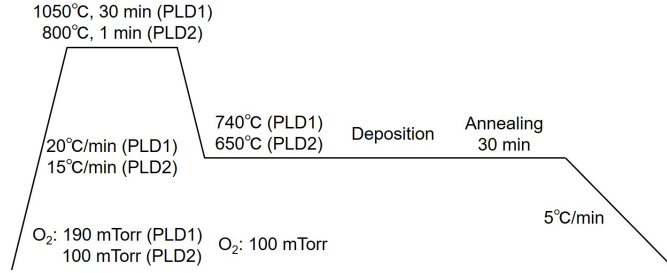


Figure 2.3: Typical procedure for deposition

terrace structure. The substrates were fixed on Inconel® plates during film deposition.

For film growth, we used MC-LMBE systems (Pascal Co., Ltd.) and KrF excimer laser COMPexPro102 with wavelength 248 nm (Coherent Inc.). We used two chambers with different heating systems, PLD1 with laser heating and PLD2 with lamp heating. The chambers for deposition were always kept in $10^{-8} - 10^{-9}$ Torr by turbomolecular pumps, which enables film synthesis in a clean environment.

Typical procedure for deposition is described below (Fig. 2.3). After introducing the substrate into the PLD chamber, the substrate was heated at high temperature (typically 1050°C for PLD1 and 850°C for PLD2) in ~ 0.1 Torr O_2 atmosphere to obtain clean surface. Then, the substrate was cooled down to temperature for deposition (typically 740°C for PLD1 and 650°C for PLD2) and exposed to plasma plumes of laser ablation from the PLD target caused by laser pulses. After the deposition, the sample was cooled down to room temperature in oxygen filled PLD chamber and then ejected outside for measurements.

Thickness of thin films were estimated by X-ray reflectivity as explained later. Typical thickness of $SrIr_{1-x}Sn_xO_3$ films is ~ 15 nm, and that of $CaIr_{1-x}Sn_xO_3$ films is ~ 10 nm. For $CaIr_{1-x}Sn_xO_3$ films, some samples were made with thickness ~ 20 nm to investigate thickness dependence and transport properties in the high resistivity region.

2.2 Evaluation of samples

2.2.1 Stoichiometry

We use molar ratio of Ir and Sn mixed to make PLD targets to index substitution ratio of samples. For $SrIr_{0.8}Sn_{0.2}O_3$ / $SrTiO_3(001)$, we checked stoichiometry of

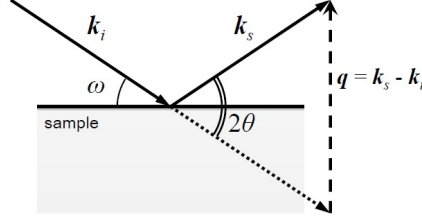


Figure 2.4: Set-up for XRD. ω is the angle between incident X-ray and substrate plane (calculated from substrate diffraction). 2θ is the angle between incident X-ray and detector.

the sample by X-ray photoemission spectroscopy (XPS). The XPS measurement was performed at BL-2A, PF, KEK., We thank Prof. Dr. Hiroshi Kumigashira, Prof. Dr. Koji Horiba, Dr. Miho Kitamura and Dr. Ryu Yukawa (KEK) for the XPS measurement.

2.2.2 X-ray diffraction and X-ray reflectivity

Phase identification and evaluation of crystalline quality of thin film samples were done based on results of X-ray diffraction (XRD) measurements, especially 2θ - θ scanning and rocking curve scanning. Reciprocal space mapping techniques were also used to investigate in-plane lattice and crystalline orientation of films. Thickness of films was estimated from X-ray reflectivity (XRR) measurement. We used SmartLab (Rigaku Corporation) using $K_{\alpha 1}$ radiation of Cu with wavelength 1.5406 \AA as X-ray source.

XRD: 2θ - θ Scan

2θ - θ scan measures intensity of diffracted X-ray in the set-up of Fig. 2.4 by changing 2θ with fixing ω to half of 2θ . This means putting the scattering vector \mathbf{q} perpendicular to the substrate plane. Therefore, 2θ - θ scan investigates stacking periodicity of film and out-of-plane lattice constant d .

XRD: reciprocal space mapping

In case lattice vectors \mathbf{a}_1 , \mathbf{a}_2 and \mathbf{a}_3 are already known, reciprocal lattice space coordinates $h = (\mathbf{q} \cdot \mathbf{a}_1)/2\pi$, $k = (\mathbf{q} \cdot \mathbf{a}_2)/2\pi$, $l = (\mathbf{q} \cdot \mathbf{a}_3)/2\pi$ can be used as scanning parameters (reciprocal space mapping, RSM). In other words, the coordinates (h, k, l) determine the scattering vector \mathbf{q}_{hkl} , and \mathbf{q}_{hkl} determines the arrangement of incident X-ray and analyzer by the relation $\mathbf{q}_{hkl} = \mathbf{k}_s - \mathbf{k}_i$.

In RSM in this research, lattice vectors of SrTiO_3 substrate were used to define the reciprocal space.

X-ray reflectivity

In X-ray reflectivity (XRR) measurement, incident X-ray is put at low angle ($\lesssim 4^\circ$) against sample. XRR enables to estimate film thickness from interference

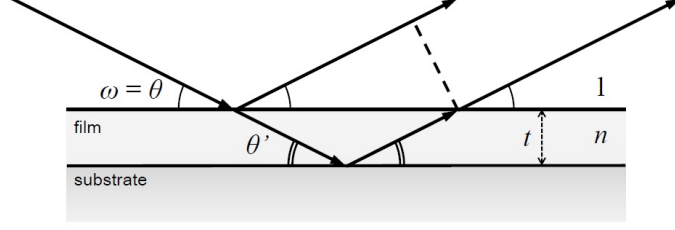


Figure 2.5: Set-up for XRR. Incident angle ω is fixed to half of the angle 2θ between incident X-ray and detector.

effect between X-ray reflected by surface of film and X-ray reflected by interface between film and substrate.

The condition in which the two reflected waves interfere and strengthen each other is given as

$$\frac{2tn \sin^2(\theta)}{\sqrt{1 - n^2 \cos^2(\theta)}} = z\lambda, \quad (2.1)$$

where t is film thickness, n is refractive index of film, λ is wavelength of incident X-ray and z is given integer. Since $n \sim 1$ for X-ray, Eq. 2.1 results in Bragg's condition.

2.2.3 Transmission electron microscope

Some $\text{CaIr}_{1-x}\text{Sn}_x\text{O}_3$ films were observed by a transmission electron microscope. I thank Dr. Daisuke Nishio-Hamane (ISSP) for the measurements. The samples for the measurements were sliced in (100) planes by an ion slicer. The measurements were done at room temperature. In addition to real space images, selected area electron diffraction were also performed in the transmission electron microscope. One snapshot of electron diffraction includes signals from typically 100 μm -long regions in the samples.

2.3 Measurement of electric transport properties

For measurement of electric transport properties, we printed Hall bar patterns on 5 mm \times 2.5 mm or 5 mm \times 5mm size samples. We used a fiber laser processing machine PLS6MW (Universal Laser System) to cut samples and print Hall bar patterns on the surfaces. For perovskite $\text{Alr}_{1-x}\text{Sn}_x\text{O}_3$ / $\text{STO}(001)$ samples, we used 5 mm \times 2.5 mm samples with edges parallel to [100] and [010] directions and printed the single Hall bar pattern (Fig. 2.6a) on it. Thus, we measured electric transport properties for a case in which the current is parallel to [100] (or [010], equivalent due to symmetry of substrate). For perovskite $\text{SrIr}_{1-x}\text{Sn}_x\text{O}_3$ / vicinal $\text{STO}(\delta 01)$ samples, we used 5 mm \times 5mm samples with edges parallel to [100] and [010] directions and printed the pattern including two Hall bars crossing perpendicularly (Fig. 2.6b) on it. Thus, we measured electric transport properties for two cases in which the current is parallel to [100] or [010]. Electric contact was obtained by contacting gold wires with 50 μm -diameter on the

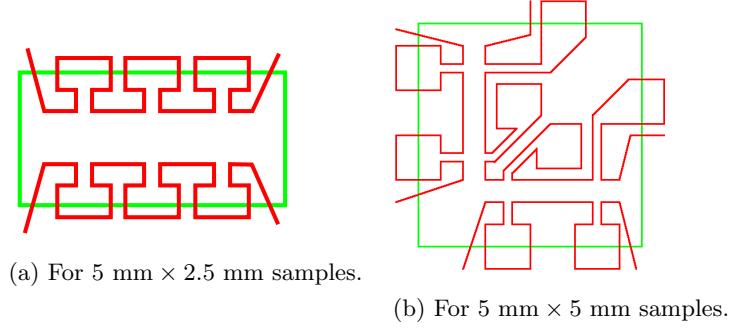


Figure 2.6: Hall bar patterns. Green boxes: outlines of the samples. Red lines: grooves printed on the surfaces of the samples by laser.



Figure 2.7: Sample with electric contact by gold wires.

surface of the sample and putting drops of silver epoxy paste over the contacts (Fig. 2.7).

We used a Physical Properties Measurement System (PPMS, Quantum Design) for the measurement.

2.3.1 Electric resistivity

Electric resistivity of samples was measured by the four-terminal method which takes I_{\pm} electrodes to introduce current and V_{\pm} electrodes separately to remove effects of resistance at interface between sample surface and wires (Fig. 2.8). We took an average of two scans with opposite directions by using AC drive mode of PPMS software to remove offset of measurements.

Resistivity of the sample ρ is calculated from the measured resistance R by the formula

$$\rho_{xx} = R_{xx} \frac{Wt}{L} = \frac{V}{I} \frac{Wt}{L} \quad (2.2)$$

where L is length between V_{\pm} electrodes in the Hall bar pattern, W is width of the Hall bar pattern and t is film thickness estimated from the XRR result.

2.3.2 Hall effect

When current with density j travels through the material along perpendicular direction to external magnetic field B , Hall effect causes electric field E along $j \times B$ direction. Hall coefficient R_H , quantity for strength of Hall effect, is given

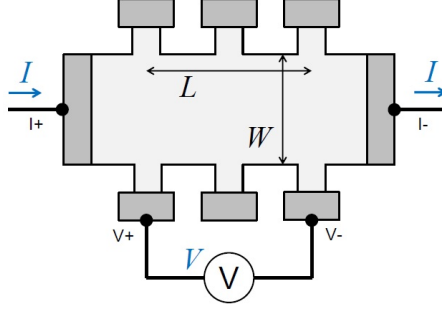


Figure 2.8: Schematic picture of setup to measure resistivity of a sample using four-terminal method.

by the formula

$$R_H = \frac{E_y}{j_x B_z} \quad (2.3)$$

when current parallel to x and magnetic field parallel to z . R_H depends on signs of charges, densities and mobilities of conducting carriers. Thus, measurements of Hall effect provide information about carries.

The Hall effect corresponds to the yx component of electric resistivity tensor ρ_{ij} , which is defined as $j_i = \sum_j \rho_{ij} E_j$. R_H is calculated from ρ_{yx} by the equation $\rho_{yx} = R_H B_z$.

In case the material has only one kind of carrier, R_H is given by the equation

$$R_H = \frac{1}{qn} \quad (2.4)$$

using charge q and number density n of the carrier. Thus, the sign of R_H reflects whether the carrier is electron or hole, and the absolute value of R_H reflects carrier density.

In case the materials have two kinds of carriers, R_H is given by the equation

$$R_H = \frac{\sigma_1^2 R_{H1} + \sigma_2^2 R_{H2} + \sigma_1^2 \sigma_2^2 R_{H1} R_{H2} (R_{H1} + R_{H2}) B^2}{(\sigma_1 + \sigma_2)^2 + \sigma_1^2 \sigma_2^2 (R_{H1} + R_{H2})^2 B^2} \quad (2.5)$$

using electric conductivity $\sigma_i = n_i e \mu_i$ and one-carrier Hall coefficient $R_{Hi} = 1/q_i n_i$ [44]. Therefore, $\rho_{yx} = R_H B$ is nonlinear at high fields. The typical scale of the field under which ρ_{yx} shows nonlinearity is $B \sim \rho/R_H$ from the condition that the first and second terms in the denominator of the equation 2.5 have similar size. At low fields, the formula becomes as follows.

$$R_H = \frac{\sigma_1^2 R_{H1} + \sigma_2^2 R_{H2}}{(\sigma_1 + \sigma_2)^2} = \frac{1}{(n_1 \mu_1 + n_2 \mu_2)^2} \left(\frac{n_1 \mu_1^2}{q_1} + \frac{n_2 \mu_2^2}{q_2} \right). \quad (2.6)$$

R_H depends on carrier mobilities μ_i . A carrier with large carrier density or mobility has a large effect on R_H . When one carrier has much higher mobility than the other, the carrier with high mobility dominates R_H because of μ^2 contribution. When both electron and hole carriers coexist, cancellation of their contributions makes $|R_H|$ smaller.

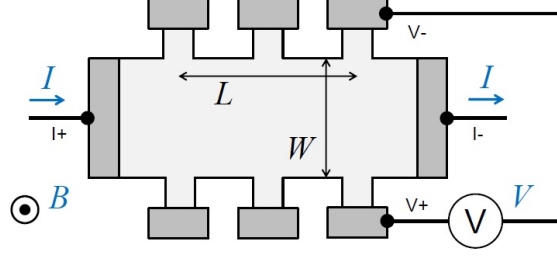


Figure 2.9: Schematic picture of setup to measure ρ_{yx} of a sample.

For ferromagnetic materials, an additional term proportional to magnetization M_z sometimes appears in ρ_{yx} :

$$\rho_{yx} = R_H B_z + R_{\text{AHE}} M_z. \quad (2.7)$$

This effect is called the anomalous Hall effect [10].

In this research, Hall resistance was measured by using above-mentioned Hall bar patterns as displayed in Fig. 2.9. ρ_{yx} is obtained by multiplying film thickness estimated from XRR on ρ_{yx} .

ρ_{yx} has typically 1/100 or smaller size of ρ_{xx} . To eliminate offset and contamination of ρ_{xx} from ρ_{yx} data, we used this way for $\text{AlIr}_{1-x}\text{Sn}_x\text{O}_3$ films, which may be magnetic. First, the sample was cooled at the maximum external field (typically +9 T) down to minimum temperature (typically 2 K). Then, field sweeping measurements to the opposite field (−9 T) was done, and the data $\rho_{yx}^{\text{down}}(B_z)$ was obtained. After that, field sweeping measurements to the initial field (+9 T) was done, and the data $\rho_{yx}^{\text{up}}(B_z)$ was obtained. Then the sample was heated up to the next temperature and similar down- and up-sweeping measurement was done for each temperature. The final data $\rho_{yx}(B_z)$ is obtained from $\rho_{yx}^{\text{down}}(B_z)$ and $\rho_{yx}^{\text{up}}(B_z)$ by the equation $\rho_{yx}(B_z) = [\rho_{yx}^{\text{down}}(B_z) - \rho_{yx}^{\text{up}}(-B_z)]/2$. This method returns the proper results when ferro-magnetization flips completely during the down- and up-sweepings.

2.4 Measurement of magnetism

2.4.1 Magnetization

In this research, we measured magnetization of the samples by SQUID magnetometer, by using Magnetic Properties Measurement System (Quantum Design). The data of magnetization include background like a diamagnetic moment from SrTiO_3 and ferromagnetic impurity contaminated during synthesis. The magnetization of a bare STO substrate similarly processed to PLD synthesis is shown in Fig. 2.10. The ferromagnetic impurity probably comes from Inconel® onto the backside surface of the substrate. Since these backgrounds show no anomaly in temperature range for measurement, magnetic transitions observed in the samples are attributed to the thin films.

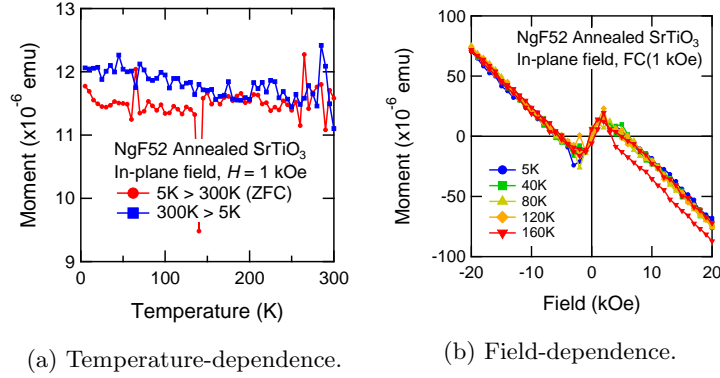


Figure 2.10: Magnetization of SrTiO_3 substrate heated in the same sequence as film syntheses in the PLD1 chamber. Magnetic field was applied along in-plane direction.

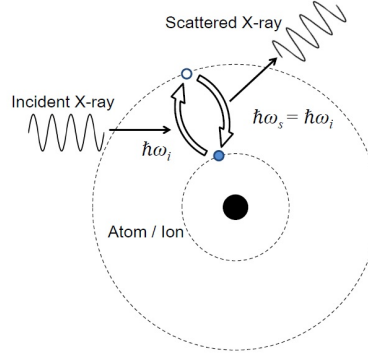


Figure 2.11: Illustration of concept of resonant elastic X-ray scattering.

2.4.2 Magnetic diffraction using resonant X-ray scattering

In this research, we investigated the magnetic structure of $\text{SrIr}_{1-x}\text{Sn}_x\text{O}_3$ by diffraction measurements using resonant X-ray scattering (RXS) technique. The experiment was performed in BL19LXU in SPring-8 [45] with help of Dr. Hiroyuki Ohsumi (RIKEN SPring-8 center). We also thank Prof. Dr. Takahisa Arima for discussion and planning of the experiment.

RXS is the scattering process of photons incoming to a material where an electron in the material excites to high energy level with absorption of an incident photon and then the electron moves to low energy level with emission of a scattered photon. In case the excited electron goes back to the initial state, it is especially called resonant elastic X-ray scattering or REXS (Fig. 2.11). Measurement of RXS provides information about filled and unfilled energy levels of electrons in the material. In particular, diffraction of X-ray scattered by the REXS process provides information about order of electronic states on each atomic site in materials.

Form factor of REXS depends on directions of polarization of an incident photon (α) and a scattered photon (β), where α and β are defined as directions

of the electric field of the photons. Form factor tensor $f_{\alpha\beta}$ is given as

$$f_{\alpha\beta} = \sum_{i,m} m_e \omega_{im}^2 \frac{\langle i | \hat{R}_\beta | m \rangle \langle m | \hat{R}_\alpha | i \rangle}{\hbar\omega - \hbar\omega_{im} + i\eta} \quad (2.8)$$

under the electric dipole approximation, where $|i\rangle$ is an initial state of the electron, $|m\rangle$ is an excited state of the electron, $\hbar\omega_{im}$ is difference between the energies of $|i\rangle$ and $|m\rangle$, $\hbar\omega$ is the energy of the incident photon, and \hat{R}_ν is the position operator along ν direction [46].

For iridates with the $J_{\text{eff}} = 1/2$ state, diffraction of REXS at the L_3 edge of iridium¹ provides information about magnetic orders formed by the $J_{\text{eff}} = 1/2$ pseudo-spins [12].

In REXS at the L_3 of iridium, the initial state $|i\rangle$ is one of four $2p_{3/2}$ states

$$\left| j = \frac{3}{2}, j_z = \pm \frac{3}{2} \right\rangle = \frac{1}{\sqrt{2}} (\mp |2p_x, \pm\sigma\rangle - i |2p_y, \pm\sigma\rangle), \quad (2.9)$$

$$\left| j = \frac{3}{2}, j_z = \pm \frac{1}{2} \right\rangle = \frac{1}{\sqrt{6}} (\mp |2p_x, \mp\sigma\rangle - i |2p_y, \mp\sigma\rangle + 2 |2p_z, \pm\sigma\rangle). \quad (2.10)$$

The excited state $|m\rangle$ is the unfilled one of two $j_{\text{eff}} = 1/2$ states

$$\left| j_{\text{eff}} = \frac{1}{2}, j_{\text{eff}z} = \pm \frac{1}{2} \right\rangle = \frac{1}{\sqrt{3}} (|5d_{xy}, \mp\sigma\rangle \mp |5d_{yz}, \pm\sigma\rangle + i |5d_{zx}, \pm\sigma\rangle). \quad (2.11)$$

$\sum \langle i | \hat{R}_\beta | m \rangle \langle m | \hat{R}_\alpha | i \rangle$, the factor of $f_{\alpha\beta}$ which depends on $|m\rangle$ is calculated as

$$\sum_{j_z = -3/2}^{+3/2} \left\langle j = \frac{3}{2}, j_z \left| \hat{R}_\beta \right| m \right\rangle \left\langle m \left| \hat{R}_\alpha \right| j = \frac{3}{2}, j_z \right\rangle = I^2 \begin{pmatrix} 2/3 & \pm i/3 & 0 \\ \mp i/3 & 2/3 & 0 \\ 0 & 0 & 2/3 \end{pmatrix} \quad (2.12)$$

$$\text{for } |m\rangle = \left| j_{\text{eff}} = \frac{1}{2}, j_{\text{eff}z} = \pm \frac{1}{2} \right\rangle$$

where $I = \langle 5d_{xy} | x | 2p_y \rangle = \langle 5d_{xy} | y | 2p_x \rangle = \langle 5d_{yz} | y | 2p_z \rangle = \dots$.

The equation 2.12 says that the y -polarized component of the scattered photons has two possible different phases depending on which of $j_{\text{eff}z} = \pm 1/2$ the excited state is. In case the $J_{\text{eff}} = 1/2$ pseudo-spin has non-zero expected values of magnetic moment, occupancy probabilities of $j_{\text{eff}z} = \pm 1/2$ states differ, and photons may scatter with polarization perpendicular to the incident photons. These scattered photons have dependency of phase and intensity on the direction of the expected value of the magnetic moment. Therefore, REXS diffraction reflects magnetic orders of $j_{\text{eff}z} = \pm 1/2$ pseudo-spins when component of the scattered X-ray with polarization perpendicular to the incident X-ray.

In this research, magnetic diffraction measurements on a $\text{SrIr}_{0.8}\text{Sn}_{0.2}\text{O}_3$ / STO(001) sample were performed using the L_3 edge REXS of iridium. Reciprocal space mapping and energy scanning were performed with $\sigma - \sigma'$ and $\sigma - \pi'$

¹Spin orbit coupling splits $2p$ orbitals to two energy levels, the low energy level $2p_{1/2}$ and the high energy level $2p_{3/2}$. Excitations from $2p_{1/2}$ to d orbitals are called as the L_2 edge and excitations from $2p_{3/2}$ to d orbitals are called as the L_3 edge.

configurations in which components with polarization parallel and perpendicular to the incident X-ray. The measurements were mainly done at 125 K, lower temperature than the magnetic transition temperature 180 K. The temperature-dependence of the magnetic diffraction found around $(1/2, 1/2, 1/2)_{\text{STO}}$ was also investigated from 110 K to 210 K.

Chapter 3

Results and Discussion

3.1 Structural evaluation

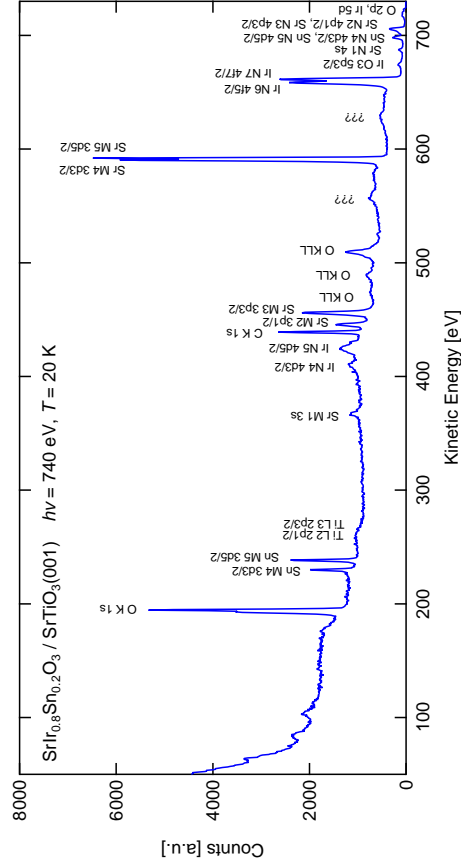
3.1.1 Stoichiometry

We performed X-ray photoemission spectroscopy (XPS) measurement on $\text{SrIr}_{0.8}\text{Sn}_{0.2}\text{O}_3$ thin film. Fig. 3.1 shows the XPS spectrum. Comparing intensities of photoemission peaks of Ir $4f$ orbits and Sn $4d$ orbits normalized by photoemission cross sections estimated based on the literature [5], substitution ratio of Sn is estimated as $x \sim 0.21(5)$. This estimation of x agrees with molar ratio of Ir and Sn for target synthesis, 0.2. Of course, we should have checked stoichiometry for several samples with various x in order to obtain accurate indexing of substitution ratio. In this paper, we use molar ratio of Ir and Sn for target synthesis to index substitution ratio, but this definition may include $\sim \pm 25\%$ systematic error at most.

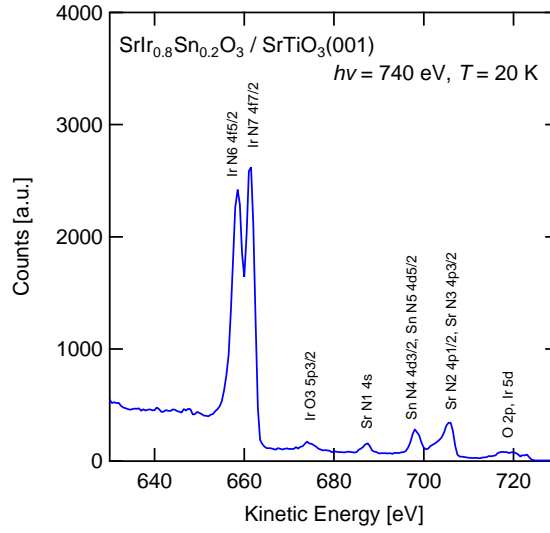
3.1.2 Orthorhombic perovskite SrIrO_3

Fig. 3.2 shows results of XRD 2θ - θ scans of $\text{SrIr}_{1-x}\text{Sn}_x\text{O}_3$ films ($x = 0, 0.2$) on vicinal $\text{STO}(\delta 01)$ substrates. Film peaks are found near sharp $00n_{\text{STO}}$ peaks, identified as pseudo-cubic $00n$ diffraction of the perovskite phase of SrIrO_3 . The out-of-plane lattice constant of SrIrO_3 films, $\sim 4.0 \text{ \AA}$ at $x = 0$, increases by $\sim 1\%$ by 20% substitution of Ir by Sn, reflecting their different ionic radii (see Fig. 3.3.). Laue oscillation around film peaks, which indicates well established film thickness, is observed for $x = 0.2$, but not for $x = 0$. We are not sure about the reasons at the moment. Perhaps we should have found good conditions for synthesis more precisely for each substitution level. The results of XRD reciprocal space mapping around 103_{STO} and 013_{STO} show that the in-plane lattices of both undoped and doped films are fixed to the substrate along both $[100]$ and $[010]$ directions (see Fig. 3.4.).

Previous studies show that perovskite SrIrO_3 grows on $\text{STO}(001)$ surface with c parallel to $[100]$ or $[010]$ ([32], Fig. 3.5a). Dr. Naoka Hiraoka had checked by XRD RSM that this relationship of crystalline orientation is also the case for Sn-doped SrIrO_3 / $\text{STO}(001)$ films (Fig. 3.6). The results show that $\text{SrIr}_{0.8}\text{Sn}_{0.2}\text{O}_3$ / $\text{STO}(001)$ film has a diffraction from the film around $0\ 1\ 5/2_{\text{STO}}$ while no film peak is observed around $0\ 1/2\ 2_{\text{STO}}$. Therefore, c axis



(a) From 50 eV to 730 eV.



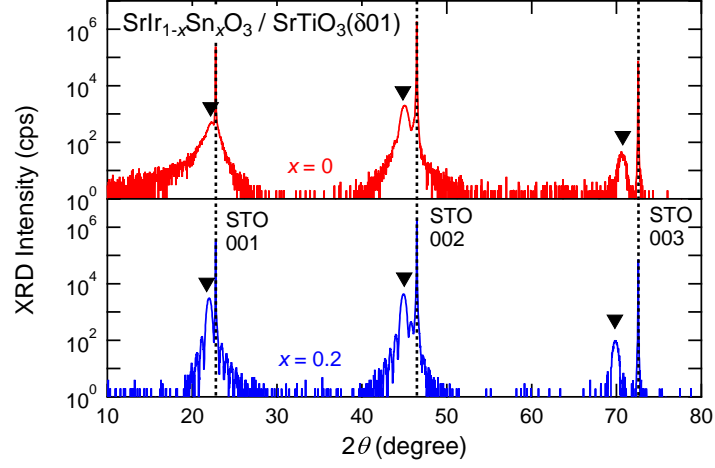


Figure 3.2: XRD 2θ - θ scan of perovskite $\text{SrIr}_{1-x}\text{Sn}_x\text{O}_3$ / $\text{SrTiO}_3(\delta 01)$ films.

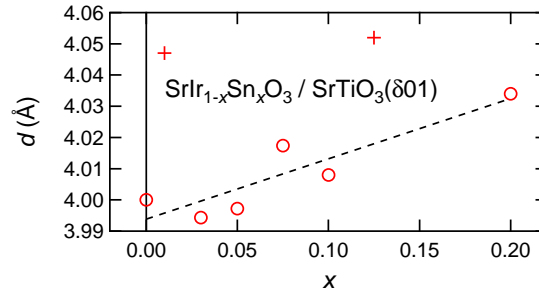


Figure 3.3: Out-of-plane lattice constant of perovskite $\text{SrIr}_{1-x}\text{Sn}_x\text{O}_3$ / $\text{SrTiO}_3(\delta 01)$ films. Dashed line: linear fitting of the data excluding $x = 0.01$ and 0.125 as outliers.

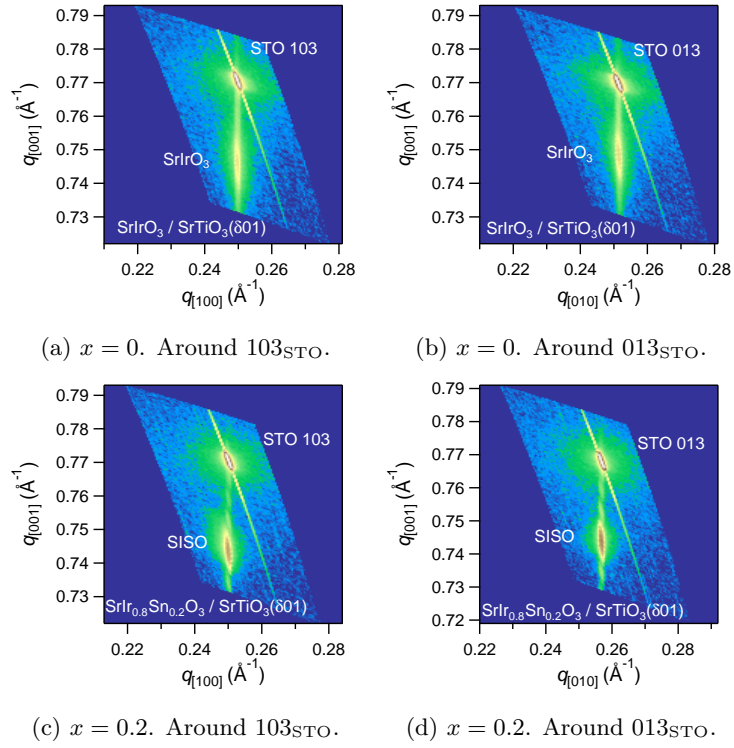


Figure 3.4: XRD reciprocal space mapping of perovskite $\text{SrIr}_{1-x}\text{Sn}_x\text{O}_3$ / $\text{SrTiO}_3(\delta 01)$ films.

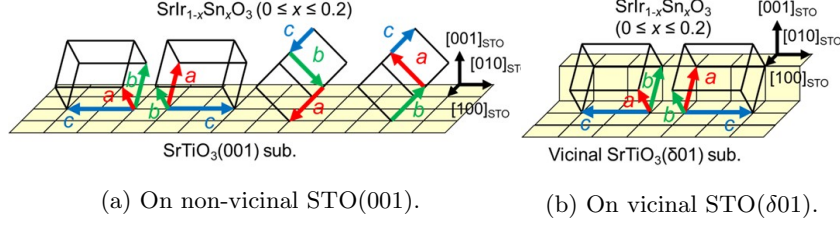


Figure 3.5: Schematic pictures of crystalline orientation of SrIr_{1-x}Sn_xO₃ films on SrTiO₃ substrates.

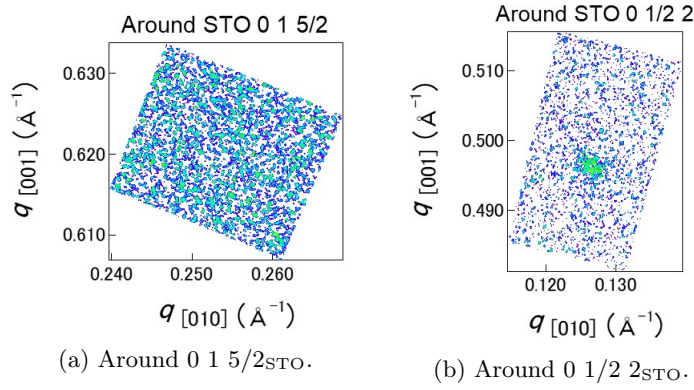


Figure 3.6: XRD reciprocal space mapping of perovskite SrIr_{0.8}Sn_{0.2}O₃ / SrTiO₃(001) film.

of perovskite SrIr_{1-x}Sn_xO₃, which has two-fold periodicity of the pseudo-cubic unit cell, lies along [010]_{STO} direction, and no or negligibly small part of the film has $c \parallel [001]$. Considering the four-fold rotational symmetry of STO(001) plane, domains with $c \parallel [100]$ should also exist as well as $c \parallel [010]$. For SrIr_{1-x}Sn_xO₃ films grown on vicinal STO(δ01) substrates, we compared the intensity of XRD reflections around STO 1/2 0 2 and 0 1/2 2 (Fig. 3.7). The results show that, for both $x = 0$ and 0.2, the intensity at 0 1/2 2 is significantly larger than that of 1/2 0 2, which means that a major part of the domains has c axis along [010] (Fig. 3.5b). We estimate from the intensities that more than 95 % of domains in film have crystalline orientation $c \parallel [010]$ _{STO}.

3.1.3 Orthorhombic perovskite CaIrO₃

Fig. 3.8 show results of XRD 2θ-θ scans of CaIr_{1-x}Sn_xO₃ films. Pseudo-cubic diffraction peaks of perovskite CaIrO₃ phase are found around sharp STO 00*n* peaks. Peak intensities of films are weaker mainly due to smaller thickness. Out-of-plane lattice constant of CaIrO₃ films increases by Sn doping like SrIrO₃ (Fig. 3.9). In-plane lattice is fixed to STO substrate both for undoped and doped films (Fig. 3.10).

It is known that perovskite CaIrO₃ film grows on STO(001) substrate with c perpendicular to the (001) plane ([23], Fig. 3.11a). We found that this selectivity of crystalline orientation is broken in Sn-doped CaIrO₃ films by observation

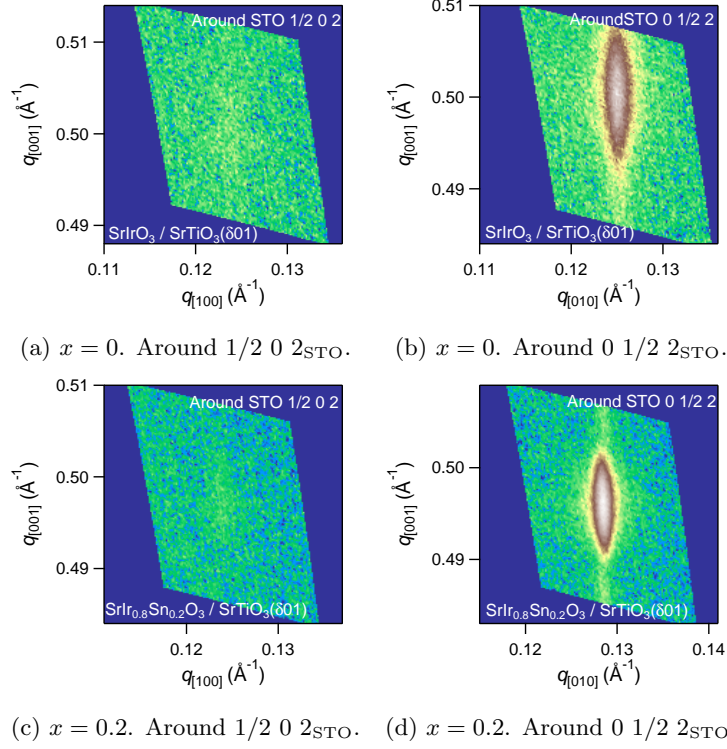


Figure 3.7: XRD reciprocal space mapping of perovskite $\text{SrIr}_{1-x}\text{Sn}_x\text{O}_3$ / $\text{SrTiO}_3(\delta 01)$ films.

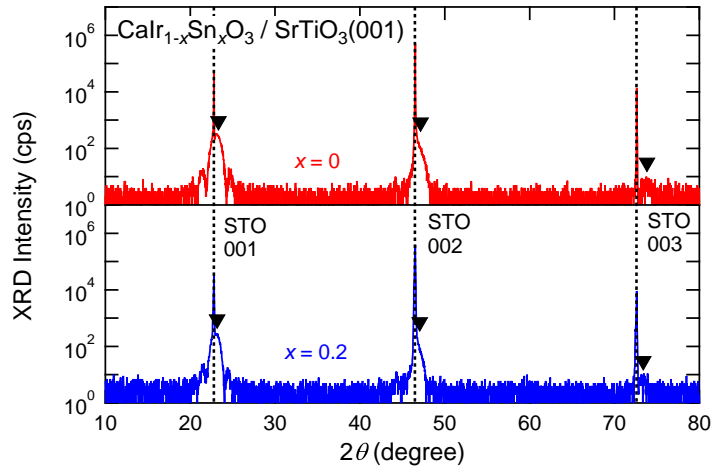


Figure 3.8: XRD 2θ - θ scan of perovskite $\text{CaIr}_{1-x}\text{Sn}_x\text{O}_3$ / $\text{SrTiO}_3(\delta 01)$ films.

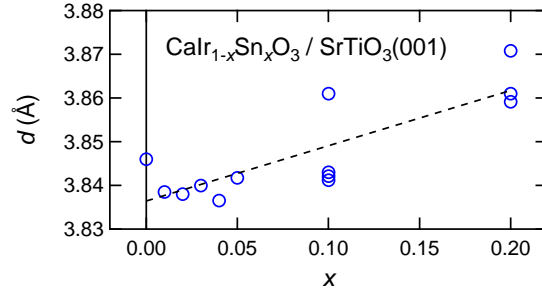


Figure 3.9: Out-of-plane lattice constant of perovskite $\text{CaIr}_{1-x}\text{Sn}_x\text{O}_3$ / $\text{SrTiO}_3(\delta 01)$ films. Dashed line: linear fitting of the data.

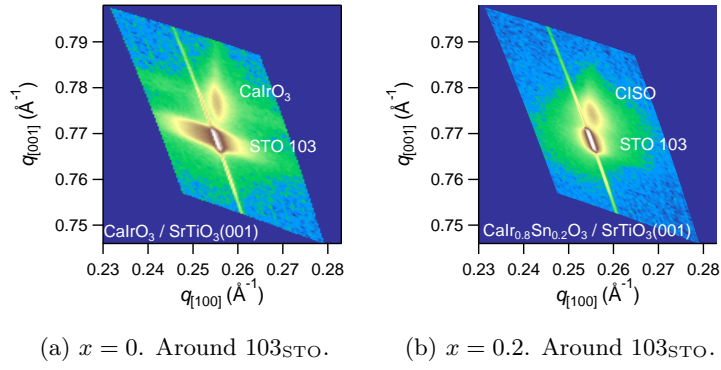


Figure 3.10: XRD reciprocal space mapping of perovskite $\text{CaIr}_{1-x}\text{Sn}_x\text{O}_3$ / $\text{SrTiO}_3(001)$ films.

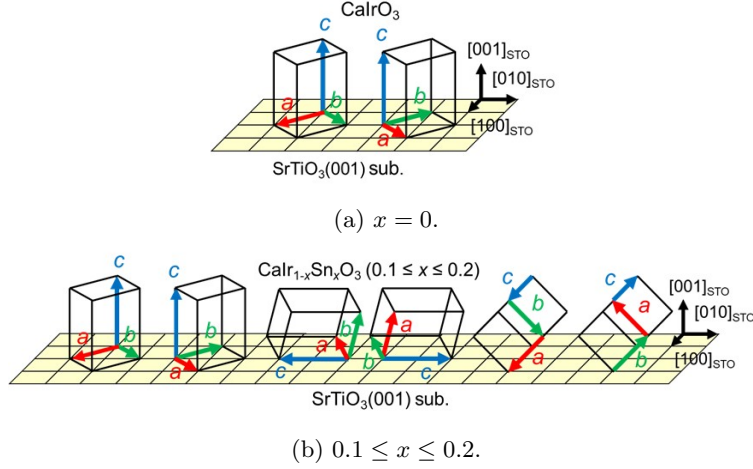


Figure 3.11: Schematic pictures of crystalline orientation of $\text{CaIr}_{1-x}\text{Sn}_x\text{O}_3$ films on $\text{SrTiO}_3(001)$ substrates.

Table 3.1: The bulk lattice parameters of SrIrO_3 and CaIrO_3 and their matching to the cubic lattice parameter of SrTiO_3 ($a_{\text{STO}} = 3.905 \text{ \AA}$).

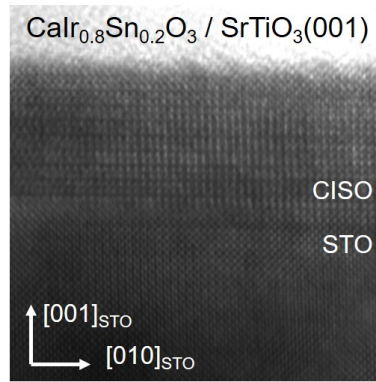
	a	b	c	$\frac{a_{\text{pc}}}{a_{\text{STO}}} - 1$	$\frac{c_{\text{pc}}}{a_{\text{STO}}} - 1$
SrIrO_3 [25]	$5.597(1) \text{ \AA}$	$5.581(1) \text{ \AA}$	$7.752(2) \text{ \AA}$	+1.2 %	−0.7 %
CaIrO_3 [14]	$5.3597(5) \text{ \AA}$	$5.6131(4) \text{ \AA}$	$7.6824(8) \text{ \AA}$	−0.6 %	−1.6 %

using a transmission microscope (Fig 3.12). Selected area electron diffraction on $\text{CaIr}_{1-x}\text{Sn}_x\text{O}_3 / \text{STO}(001)$ samples ($x = 0.1$ shown in Fig. 3.12b, $x = 0.2$ not shown) shows superlattice diffraction spots with double periodicity of pseudocubic perovskite lattice along both in-plane and out-of-plane directions (notated as $[010]$ and $[001]$ in the figure). Considering that GdFeO_3 -type distortion makes unit cell $\sqrt{2} \times \sqrt{2} \times 2$ times larger than cubic perovskite, diffraction spots at (0, integer, half-integer) come from domains with $c \parallel [001]$, (0, half-integer, integer) from $c \parallel [010]$, and (0, half-integer, half-integer) from $c \parallel [100]$, respectively. Therefore, doped CaIrO_3 films also have domains with c in-plane, in addition to domains with c out-of-plane (undoped systems), as illustrated in Fig. 3.11b.

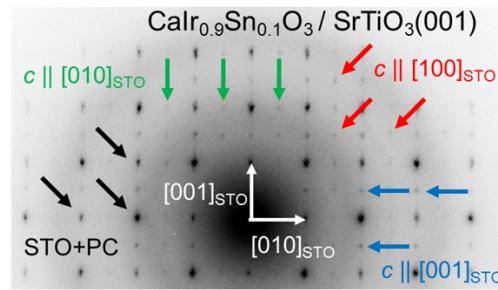
3.1.4 Discussion

Relationship of crystalline orientations of perovskite AIrO_3 films on $\text{STO}(001)$ is explained by matching of bulk lattice constants. Reported values of lattice constants of perovskite AIrO_3 and their matching to STO are shown in Table 3.1. a_{pc} and c_{pc} in the Table are given by the equations $a_{\text{pc}} = \sqrt{a^2 + b^2}/2$ and $c_{\text{pc}} = c/2$.

In SrIrO_3 on $\text{STO}(001)$, the c axis of the orthorhombic perovskite-type unit cell, which has better matching to STO than the ab plane, lies parallel to $[100]$ and $[010]_{\text{STO}}$. In SrIrO_3 on vicinal $\text{STO}(\delta 01)$, epitaxial strain works from both the bottom (001) and side (100) planes near steps, and aligns the c axis parallel



(a) Real space image ($x = 0.2$).



(b) Selected area electron diffraction ($x = 0.1$).

Figure 3.12: Observation of $\text{CaIr}_{1-x}\text{Sn}_x\text{O}_3 / \text{SrTiO}_3(001)$ films by transmission electron microscope.

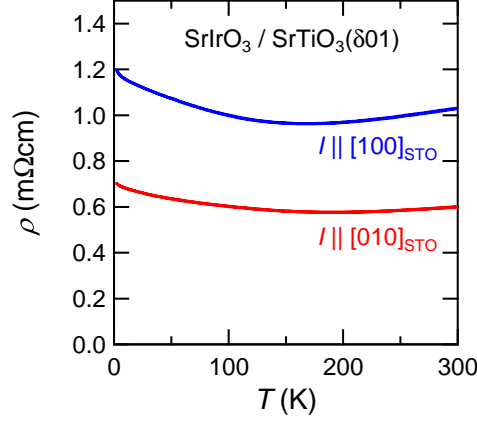


Figure 3.13: Temperature-dependent resistivity of perovskite SrIrO_3 / $\text{SrTiO}_3(\delta 01)$ film.

to $[010]$. These relationships of crystalline orientations are not changed by Sn doping, because the c axis remains to have better matching than the ab plane.

In CaIrO_3 on $\text{STO}(001)$, on the other hand, the ab plane, which has better matching to STO than the c axis, lies parallel to $(001)_{\text{STO}}$ and the c axis aligns along $[001]_{\text{STO}}$. Sn doping increases the lattice constants of CaIrO_3 and makes c closer to STO 's a , which results in coexistence of the three crystalline orientations in doped films.

3.2 Semimetallic properties of undoped systems

3.2.1 Orthorhombic perovskite SrIrO_3

Fig. 3.13 shows temperature-dependence of perovskite SrIrO_3 thin film. Resistivity is almost temperature-independent. For detail, it gradually decreases as temperature decreases from room temperature down to ~ 170 K, and then gradually increases down to 2 K. Upturn of $\rho(T)$ at low temperature is very small in the range we measured. Therefore insulating behavior at low temperature comes from other factors from a band gap, like localization, etc. Or, even if it comes from a band gap, the gap size is estimated to be in smaller order than 1 meV.

Resistivity with current parallel to $[010]$ is lower than that with current parallel to $[100]$. This difference has two possible origins. The first is that the anisotropic resistivity reflects the anisotropic electronic state of SrIrO_3 . The second possible reason is anisotropy of crystalline quality in the sample. $\text{SrIr}_{1-x}\text{Sn}_x\text{O}_3$ samples on vicinal $\text{STO}(\delta 01)$ surface are supposed to have lower crystalline quality along $[100]$ direction than $[010]$ due to step-terrace structure of substrate surface, which may make crystalline distortions in the film layer.

Perovskite SrIrO_3 films have linear ρ_{yx} . Temperature-dependence of Hall coefficient R_H is displayed in Fig. 3.14. R_H is negative for all temperature range [2 K, 300 K] and $|R_H|$ increases as T decreases. Similar negative R_H -s are also

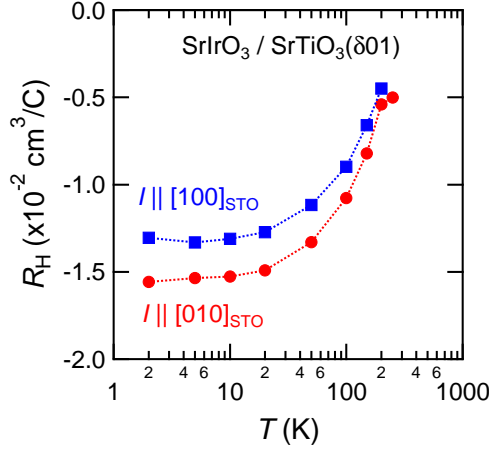


Figure 3.14: Temperature-dependent Hall coefficient of perovskite SrIrO_3 / $\text{SrTiO}_3(\delta 01)$ film.

reported in previous studies on both bulk and films [37, 30], indicating existence of electron-type carriers with high mobility, i.e. Dirac electrons in this material. Temperature-dependence is explained by increase of carrier density on Dirac and other bands due to thermal excitation.

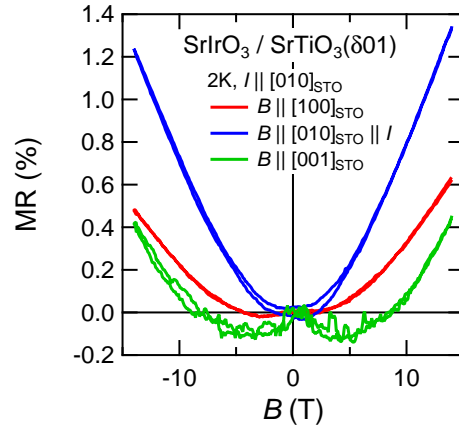
Perovskite SrIrO_3 thin film shows non-trivial anisotropy of magnetoresistance (MR). Fig. 3.15 shows MR of perovskite SrIrO_3 on vicinal $\text{STO}(\delta 01)$. The anisotropy of the MR is described as follows.

- **In case the current was applied along [010]**, the relatively strong positive MR (over 1 % at 9 T) appears when the field is along [010]. The weak positive MR with almost half magnitude is also observed when the field is along [010]. When the field is along [001], the MR turns negative at low field.
- **In case the current was applied along [100]**, the MR is positive and isotropic.

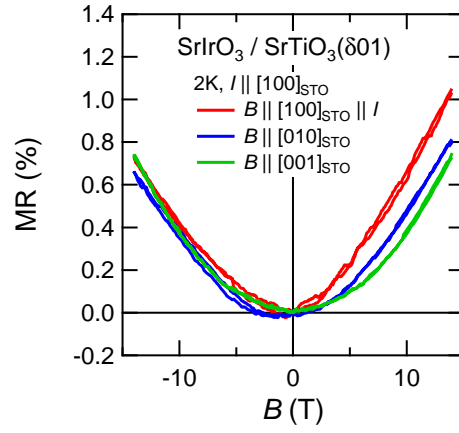
To our knowledge, this anisotropy of MR does not allow an easy interpretation. When considering only the case for $I \parallel [010]$, the MR may be broken down into the positive longitudinal MR and the negative MR caused by weak localization, which is supposed to be largest when $B \parallel [001]$ due to the sample shape of thin film. In that case, the positive longitudinal MR may be attributed to the anisotropy of electronic states of perovskite SrIrO_3 . However, this scenario would not explain the isotropic MR under $I \parallel [100]$. We just propose a hypothesis that crystal dislocations caused by step-terrace structures of the substrate may distort direction of local current density and suppress total anisotropy of MR.

3.2.2 Orthorhombic perovskite CaIrO_3

Fig. 3.16 shows temperature-dependent resistivity of perovskite CaIrO_3 thin film. The resistivity gradually increases as temperature decreases from room



(a) $I \parallel [010]_{\text{STO}}$.



(b) $I \parallel [100]_{\text{STO}}$.

Figure 3.15: Magnetoresistance of perovskite $\text{SrIrO}_3 / \text{SrTiO}_3(\delta 01)$ film.

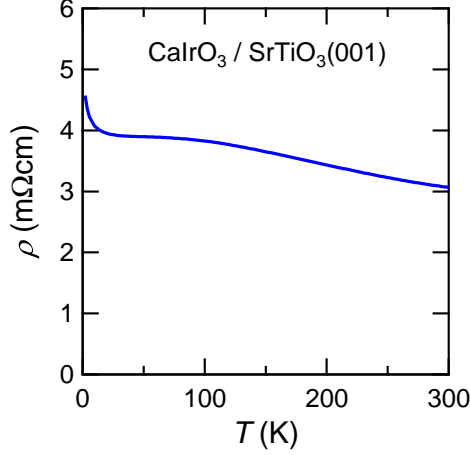


Figure 3.16: Temperature-dependent resistivity of perovskite CaIrO_3 / $\text{SrTiO}_3(001)$ film.

temperature down to ~ 100 K, then almost stays at the same value down to ~ 20 K, and shows upturn down to 2 K (bottom temperature of measurement). Since the increase of resistivity is observed only below 20 K, the ground state is identified as a semimetal or narrow gap semiconductor whose band gap is below a few milli-electron volts. In case of semimetal, upturn of resistivity at low temperature is attributed to localization effect caused by sample disorder, probably due to coexistence of different crystalline orientations in sample. CaIrO_3 shows small, almost isotropic magnetoresistance (Fig. 3.17), similarly to SrIrO_3 with current parallel to $[100]$. W-shaped MR observed when $B \parallel [001]$ supports weak localization-induced negative MR.

As shown in Fig. 3.18, CaIrO_3 shows nonlinear $\rho_{yx}(B_z)$ curve. This nonlinearity has two possible origins: multi-band effect and anomalous Hall effect. As discussed later, Sn-doped CaIrO_3 shows hysteretic $\rho_{yx}(B_z)$. Thus, the possibility of anomalous Hall effect can not be neglected though there is no clear evidence that CaIrO_3 has magnetic order at low temperature. This possibility of anomalous Hall effect makes estimation of carrier density by R_H difficult. Fig. 3.19 shows R_H -s of CaIrO_3 estimated from the slope of the $\rho_{yx}(B_z)$ curve at 0 T (low field limit) and 9 T (high field limit). The true R_H will be not far from these two limits. R_H of CaIrO_3 is positive and increases as temperature decreases, indicating hole carriers with highest mobility, probably Dirac hole band. The samples in this research do not show a sign-changing behavior as reported in the previous research [23], suggesting the level of the Dirac node is higher than the sample in the previous research, though it is still unclear which of the Fermi energy or the band dispersion changes. This disagreement of R_H also demonstrates sensitivity of carrier balance in CaIrO_3 .

3.2.3 Discussion

Carrier density and mobility of our thin film samples are summarized in Table 3.2. We also display the values reported in the previous studies on or-

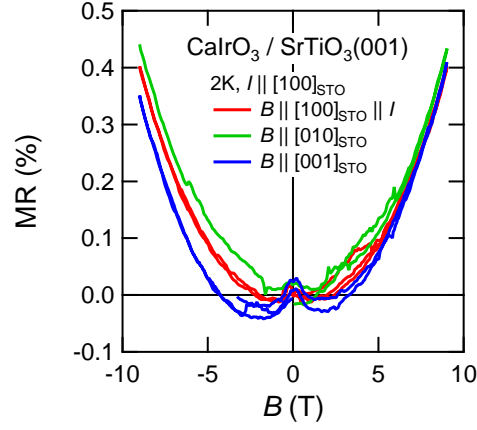


Figure 3.17: Magnetoresistance of perovskite CaIrO_3 / $\text{SrTiO}_3(001)$ film.

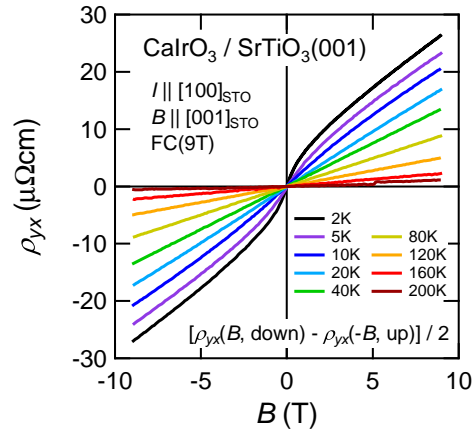


Figure 3.18: $\rho_{yx}(B_z)$ of perovskite CaIrO_3 / $\text{SrTiO}_3(001)$ film.

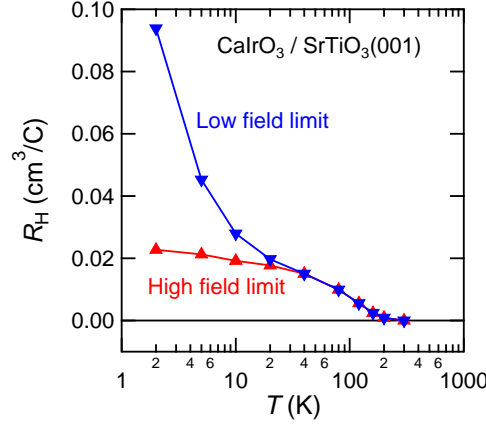


Figure 3.19: Hall coefficient of perovskite $\text{CaIrO}_3 / \text{SrTiO}_3(001)$ film.

Table 3.2: Physical quantities about electric transport at low temperature for perovskite (Pv) Sr/CaIrO_3 thin films measured in this research. Carrier density n and mobility μ are just calculated using the relations for the single carrier model, $n = 1/eR_H$ and $\mu = R_H/\rho$ (e : elementary charge). For perovskite CaIrO_3 , Hall coefficient R_H is uncertain because nonlinearity of $\rho_{yx}(B_z)$ may be caused by both multi-carrier effects and anomalous Hall effect. We ignore possible anomalous Hall effect and put the R_H and the related values estimated from the slope of $\rho_{yx}(B_z)$ at 0 T in the table. The R_H and the related values from the high field limit are put in the bracket ().

Material	Note	$\rho/\Omega\text{cm}$	$R_H/\text{cm}^3\text{C}^{-1}$	n/cm^{-3}	$\mu/\text{cm}^2\text{V}^{-1}\text{s}^{-1}$
Pv SrIrO_3	2 K, $I \parallel [010]$	7.05×10^{-4}	-1.56×10^{-2}	-4.01×10^{20}	-22.1
	2 K, $I \parallel [100]$	1.20×10^{-3}	-1.31×10^{-2}	-4.78×10^{20}	-10.9
Pv CaIrO_3	2 K	4.57×10^{-3}	$+9.38 \times 10^{-2}$	$+6.65 \times 10^{19}$	+20.5
			$(+2.28 \times 10^{-2})$	$(+2.74 \times 10^{20})$	(+4.98)

thorhombic iridium oxides for comparison (Table 3.3).

Perovskite SrIrO_3 shows electron-type carriers with $n \sim -10^{20} \text{ cm}^{-3}$ and $\mu \sim -20 \text{ cm}^2\text{V}^{-1}\text{s}^{-1}$. The carrier density is moderate and the carrier mobility is relatively high in the three, supporting the existence of the Dirac electrons.

On the other hand, perovskite CaIrO_3 shows $n \sim +10^{19} \text{ cm}^{-3}$ and $\mu \sim +20 \text{ cm}^2\text{V}^{-1}\text{s}^{-1}$ under single carrier assumption. These estimations will not be so affected by a possible anomalous Hall effect, because magnetization of undoped perovskite CaIrO_3 will be tiny even if it exists. The carrier density is the smallest in the three. This small density indicates electric transport at low temperature is dominated by a small number of holes carriers, which suggests the existence of the Dirac node right above the Fermi level.

The temperature-dependencies of resistivity of the two (Figs.3.13, 3.16) show that localization at low temperature develops from SrIrO_3 to CaIrO_3 . This development of localization suggests that large epitaxial strain may cause lattice dislocations and introduce randomness in electric conduction.

Table 3.3: Physical quantities about electric transport at low temperature for perovskite (Pv) Sr/CaIrO₃ according to the previous studies [30, 22, 14, 23]. The values in this table are roughly estimated by us from the reported graphs. PC: bulk polycrystal. SC: bulk single crystal. TF: epitaxial thin film. GSO: GdScO₃(110) substrate. LAO: LaAlO₃(001) substrate. STO: SrTiO₃(001) substrate.

Material	Note	$\rho/\Omega\text{cm}$	$R_H/\text{cm}^3\text{C}^{-1}$	n/cm^{-3}	$\mu/\text{cm}^2\text{V}^{-1}\text{s}^{-1}$
Pv SrIrO ₃	PC [30], < 20 K	$\sim 5 \times 10^{-4}$	~ -0.1	$\sim -6 \times 10^{19}$	~ -200
	TF on GSO [22], 5 K	$\sim 1 \times 10^{-3}$	$\sim -3 \times 10^{-2}$	$\sim -2 \times 10^{20}$	~ -20
Pv CaIrO ₃	SC [14], 0.12 K	$\sim 1.5 \times 10^{-3}$	~ -100	$\sim -6 \times 10^{16}$	$\sim -6 \times 10^4$
	TF on STO [23], 2 K	$\sim 6.5 \times 10^{-3}$	$\sim +0.08$	$\sim +8 \times 10^{19}$	$\sim +10$
	TF on LAO [23], 2 K	$\sim 2.5 \times 10^{-3}$	$\sim +5 \times 10^{-3}$	$\sim +1 \times 10^{21}$	$\sim +2$

Perovskite CaIrO₃ films show positive Hall effects while the previous study on bulk reported negative Hall effects [14]. These mismatches will be attributed to epitaxial stain effects. Epitaxial stain will deform band dispersion by deforming crystal structure. Therefore, the mismatches of the signs of Hall effects suggest close location of the Dirac nodes in these materials. According to the previous study of high pressure measurements on bulk, pressure deforms band structure and moves the Dirac node to lower energy [40]. Our result, the upper shift of the Dirac node caused by elongating strain of CaIrO₃ / SrTiO₃(001) thin film, is consistent with this study on pressured bulk, because elongating strain will act as negative pressure. Other properties basically reproduce the bulk results, though thin films tend to show larger carrier density and lower mobility.

The evaluations on the semimetallic properties of our thin films are summarized as follows.

- Perovskite SrIrO₃ has the Dirac electron nodes below the Fermi energy.
- Perovskite CaIrO₃ hosts more “Dirac-like” transport properties, smaller carrier density and larger mobility than SrIrO₃. These indicate a close location of the Dirac node to the Fermi level. The large strain effect changing the sign of the Hall resistivity also supports it.

3.3 Sn substitution effects: introduction of correlation / disorders

3.3.1 Orthorhombic perovskite SrIr_{1-x}Sn_xO₃

Perovskite-type SrIr_{1-x}Sn_xO₃ thin films in this study also show a weak ferromagnetic insulating phase, as well as observed in bulk. Experimental results are explained below.

Fig. 3.20 shows temperature dependence of magnetization M of SrIr_{1-x}Sn_xO₃ samples. Anomaly in $M(T)$ and arise of a weak ferromagnetic moment below the temperature of the anomaly T_c are observed above $x = 0.125$. T_c and weak

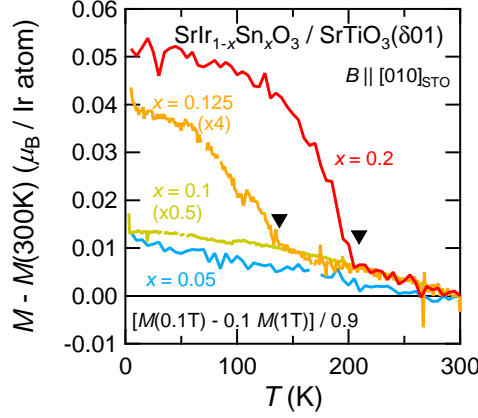
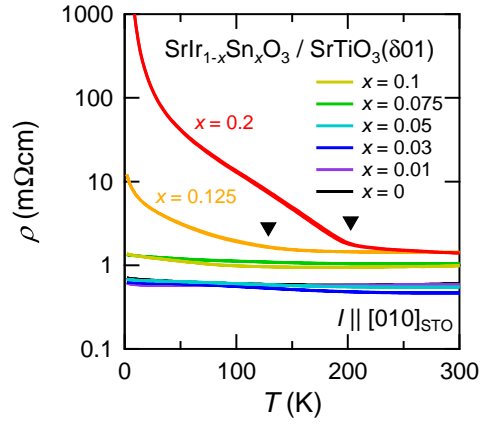


Figure 3.20: Temperature-dependent magnetization of perovskite $\text{SrIr}_{1-x}\text{Sn}_x\text{O}_3$ / $\text{SrTiO}_3(\delta 01)$ film. The values in the graph are the total magnetization of the sample divided by the number of Ir atoms in the sample, not magnetization for each Ir ions.

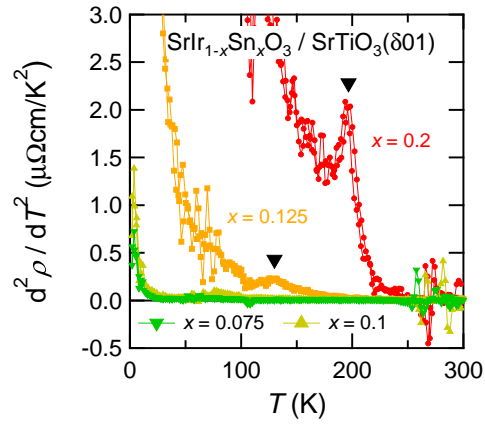
ferro-magnetization both increase as x increases to $x = 0.2$, indicating development of magnetization. The moment size per Ir sites is several percent of the $J_{\text{eff}} = 1/2$ pseudo-spin of Ir^{4+} , suggesting that this weak ferromagnetism comes from pseudo-spin canting from antiferromagnetic order. In addition, orientation control in epitaxial thin film reveals anisotropy of magnetization, which will be discussed in the later section.

Temperature-dependent resistivity (Fig. 3.21a) remains semimetallic, or almost temperature-independent, below $x = 0.1$, and also at $x = 0.125$ and 0.2 at high temperature, though value of resistivity gradually increases as x increases. At $x = 0.125$ and 0.2 , the temperature-dependent resistivity shows an anomaly, and becomes insulating below the temperature of that anomaly. These anomalies are clearly observed in the second derivative of $\rho(T)$ as displayed in Fig. 3.21b. The temperature of appearance of weak ferromagnetism in $M(T)$ data (Fig. 3.20) and the temperature of the anomaly in resistivity are plotted in Fig. 3.22, and they show good agreement for both $x = 0.125$ and 0.2 . Therefore, the weak ferromagnetism triggers the transition from semimetal to insulator.

To investigate more about Sn substitution effect on electronic state, we measured the Hall effect of $\text{SrIr}_{1-x}\text{Sn}_x\text{O}_3$ films. $\text{SrIr}_{1-x}\text{Sn}_x\text{O}_3$ films show linear $\rho_{yx}(B_z)$, and Hall coefficient is displayed in Fig. 3.23. R_H remains negative for all the measurement range, which means electrons remain the carrier with highest mobility. However, $|R_H|$ shows large x -dependence even in the semimetallic region $x \leq 0.075$. Roughly speaking, $|R_H|$ at low temperature decreases as x increases. Naïvely thinking, this means increase of carrier density of the Dirac electron band. We will discuss more about the Hall effect in the Discussion section.



(a) T -dependent resistivity.



(b) Second derivative of $\rho(T)$.

Figure 3.21: Temperature-dependent resistivity and its second derivative of $\text{SrIr}_{1-x}\text{Sn}_x\text{O}_3 / \text{SrTiO}_3(\delta 01)$ thin films.

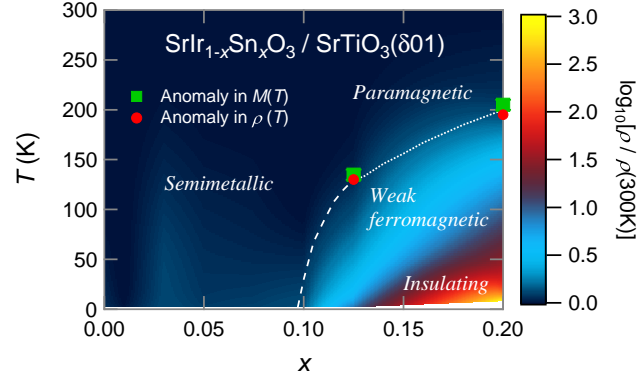


Figure 3.22: Phase diagram of $\text{SrIr}_{1-x}\text{Sn}_x\text{O}_3$ / $\text{SrTiO}_3(\delta 01)$ thin films. Color plot: Logarithmic scaled resistivity.

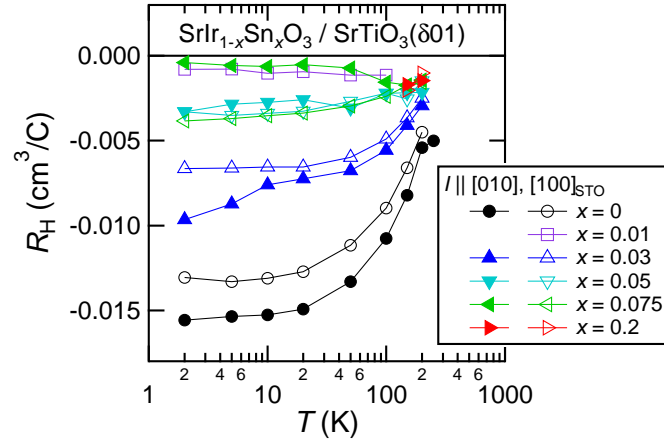


Figure 3.23: Temperature-dependent Hall coefficient of $\text{SrIr}_{1-x}\text{Sn}_x\text{O}_3$ / $\text{SrTiO}_3(\delta 01)$ thin films.

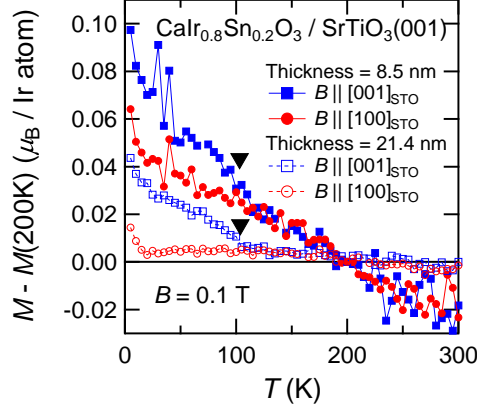


Figure 3.24: Temperature-dependent magnetization of perovskite $\text{CaIr}_{0.8}\text{Sn}_{0.2}\text{O}_3$ / $\text{SrTiO}_3(001)$ film. The values in the graph are the total magnetization of the sample divided by the number of Ir atoms in the sample, not magnetization for each Ir ions.

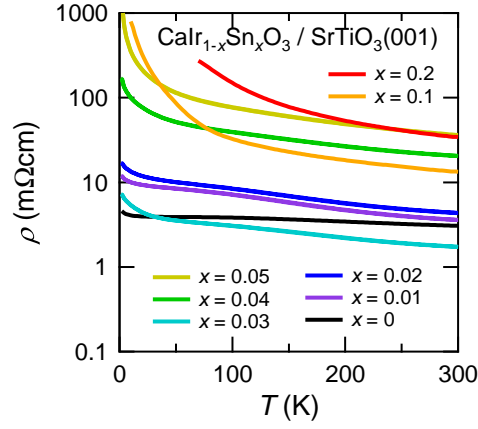
3.3.2 Orthorhombic perovskite CaIrO_3

We also investigated Sn doping effect on perovskite CaIrO_3 . We found that perovskite $\text{CaIr}_{1-x}\text{Sn}_x\text{O}_3$ films also show a weak ferromagnetic moment. However, response of electric transport property reacts differently from perovskite SrIrO_3 , suggesting different correlation / disorders effect on Dirac-semimetallic electronic state.

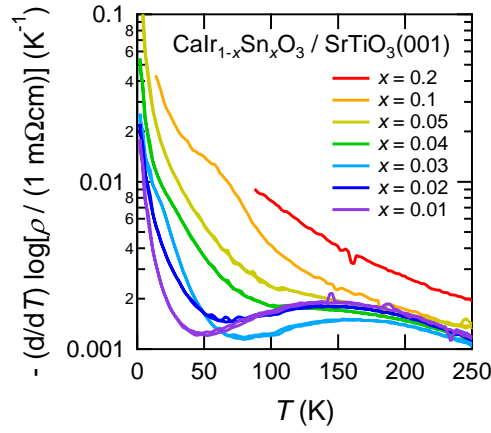
Fig. 3.24 shows temperature-dependence of magnetization of $\text{CaIr}_{0.8}\text{Sn}_{0.2}\text{O}_3$ films. For better SN ratio, data for the 20 nm-thick sample are also plotted in addition to 10 nm-thick sample. Both samples show a weak ferromagnetic moment below 100 K. In the given resolution of measurement, thickness does not affect magnetization per sample volume though detailed properties of 10 nm-thick sample is unclear due to low SN ratio. Therefore, this weak ferromagnetism comes from the bulk part of samples. Both moment size and transition temperature are lower than those of $\text{SrIr}_{0.8}\text{Sn}_{0.2}\text{O}_3$ (Fig. 3.20), indicating lower stabilization energy of weak ferromagnetism in $\text{CaIr}_{1-x}\text{Sn}_x\text{O}_3$ than $\text{SrIr}_{1-x}\text{Sn}_x\text{O}_3$.

Fig. 3.25a shows temperature-dependence of resistivity of $\text{CaIr}_{1-x}\text{Sn}_x\text{O}_3$ films. In contrast to $\text{SrIr}_{1-x}\text{Sn}_x\text{O}_3$ whose $\rho(T)$ remains semimetallic under twenty percent Sn doping, Sn doping on CaIrO_3 enhances insulating behavior in the whole temperature range from $x = 0.01$. As Sn substitution ratio x increases, more insulating $\text{CaIr}_{1-x}\text{Sn}_x\text{O}_3$ becomes. To outline development of insulating behavior, we plot derivative of $\log \rho(T)$ in Fig. 3.25b. Increase at low temperature gradually appears from higher temperature as x increases, indicating that small upturn observed at low temperature in undoped CaIrO_3 continuously develops to insulator from room temperature at $x = 0.2$. Fig. 3.26 shows the phase diagram of $\text{CaIr}_{1-x}\text{Sn}_x\text{O}_3$.

We found that resistivity of Sn doped CaIrO_3 films show large thickness dependence. Fig. 3.27 shows temperature-dependent resistivity for both 10 nm-



(a) T -dependent resistivity.



(b) Derivative of $\log \rho(T)$.

Figure 3.25: Temperature-dependent resistivity and derivative of $\log \rho$ of $\text{CaIr}_{1-x}\text{Sn}_x\text{O}_3 / \text{SrTiO}_3(01)$ thin films.

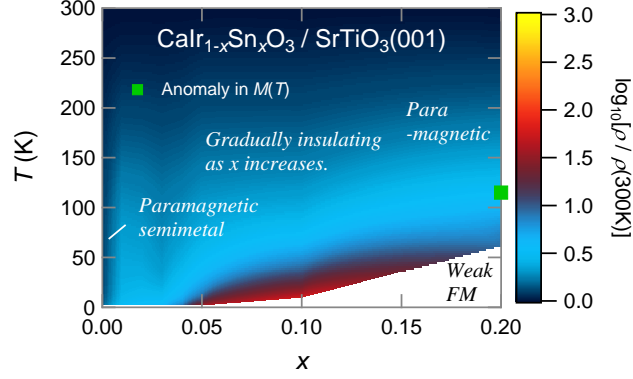


Figure 3.26: Phase diagram of $\text{CaIr}_{1-x}\text{Sn}_x\text{O}_3 / \text{SrTiO}_3(001)$ thin films. Color plot: Logarithmic scaled resistivity.

and 20 nm-thick thin films of $\text{CaIr}_{1-x}\text{Sn}_x\text{O}_3$ ($x = 0, 0.1, 0.2$). For $x \geq 0.1$, 10 nm thick samples shows higher and more insulating resistivity compared with 20 nm-thick samples. This thickness dependence indicates that lower film thickness supports the insulating behavior appearing in highly substituted region, and suggests an effect of correlation in this insulation, as discussed in 3 nm-thick SrIrO_3 thin films [38].

Like undoped CaIrO_3 , Sn doped CaIrO_3 also shows nonlinear $\rho_{yx}(B_z)$ at low temperature, as shown in Fig. 3.28. In addition, hysteresis in $\rho_{yx}(B_z)$ is observed for $x \geq 0.02$. Therefore, nonlinear $\rho_{yx}(B_z)$ may come from anomalous Hall effect, where $\rho_{yx}(B_z)$ has a term proportional to ferro-magnetization in addition to the usual Hall effect. As discussed in the Methods chapter, in case the material has two or more kinds of carriers, the usual Hall resistivity can also have nonlinearity. To separate the two terms, experimental data of the $M(B)$ curve is needed. However, extraction of the $M(B)$ curve of thin films from experimental data is difficult due to small signals from the sample and large background of data. Therefore, at the moment, we cannot divide the $\rho_{yx}(B_z)$ data into a usual Hall term and an anomalous Hall term.

To analyze how Hall effect changes as Sn substitution, we tried to separate it into linear and nonlinear parts. At first, we divided $\rho_{yx}(B_z)$ by $\rho_{xx}(B_z)^2$ to obtain $\sigma_{xy}(B_z)$ (Fig. 3.29b). Then we assumed that the slope of $\sigma_{xy}(B_z)$ in the high field region (> 8 T) indicates the linear part of $\sigma_{xy}(B_z)$, and divided $\sigma_{xy}(B_z)$ to linear and nonlinear parts (Fig. 3.29c). Figs. 3.29c, 3.30, 3.31 shows linear and nonlinear parts of $\sigma_{xy}(B_z)$ of perovskite $\text{CaIr}_{1-x}\text{Sn}_x\text{O}_3$ films ($x = 0, 0.01, 0.02, 0.03, 0.04, 0.1, 0.2$).

All $\text{CaIr}_{1-x}\text{Sn}_x\text{O}_3$ films ($0 \leq x \leq 0.2$) show nonlinear $\sigma_{xy}(B_z)$, and the temperature where nonlinearity appears becomes higher as x increases, from 20 K at $x = 0$, then 40 K at $x = 0.03$, to 120 K at $x = 0.2$. Hysteric behavior, in other words, shift of $\sigma_{xy}(B_z)$ from the origin of the graph, is observed for $x \geq 0.02$ at low temperature. The temperature where hysteresis appears is lower than that for non-linearity, 5 K for $x = 0.03$ and 40 K for $x = 0.2$. Interestingly, the shape of nonlinear $\sigma_{xy}(B_z)$ changes from S-shaped to Z-shaped as x increases. The S-shaped Hall conductivity is observed for $0 \leq x \leq 0.04$, and the Z-shaped Hall

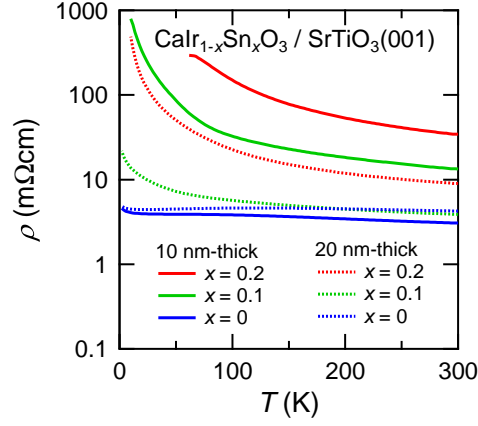


Figure 3.27: Temperature-dependent resistivity of perovskite $\text{CaIr}_{1-x}\text{Sn}_x\text{O}_3$ / $\text{SrTiO}_3(001)$ films including 20 nm thick samples. The samples with no mention about film thickness are 20 nm thick samples.

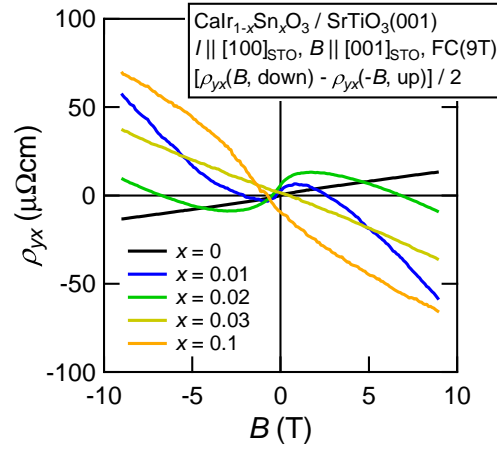


Figure 3.28: $\rho_{yx}(B_z)$ of perovskite $\text{CaIr}_{1-x}\text{Sn}_x\text{O}_3$ / $\text{SrTiO}_3(001)$ films.

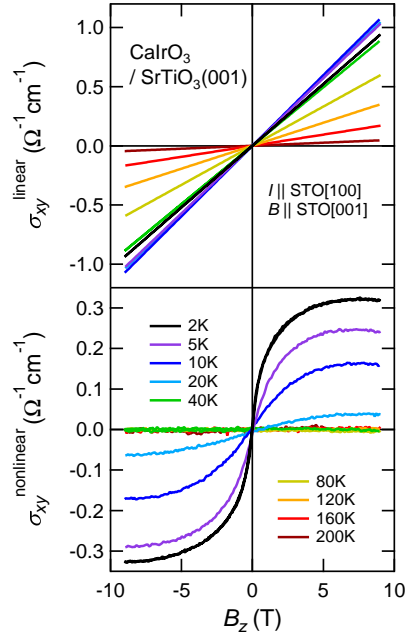
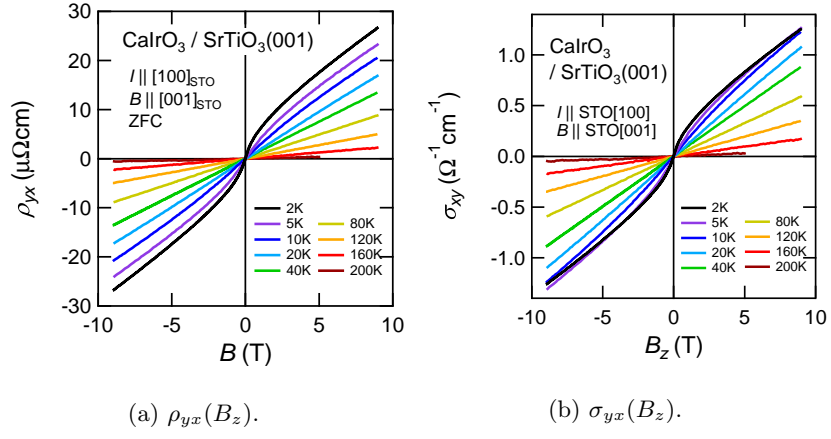


Figure 3.29: Hall resistivity $\rho_{yx}(B_z)$ and Hall conductivity $\sigma_{xy}(B_z)$ of CaIrO_3 thin film.

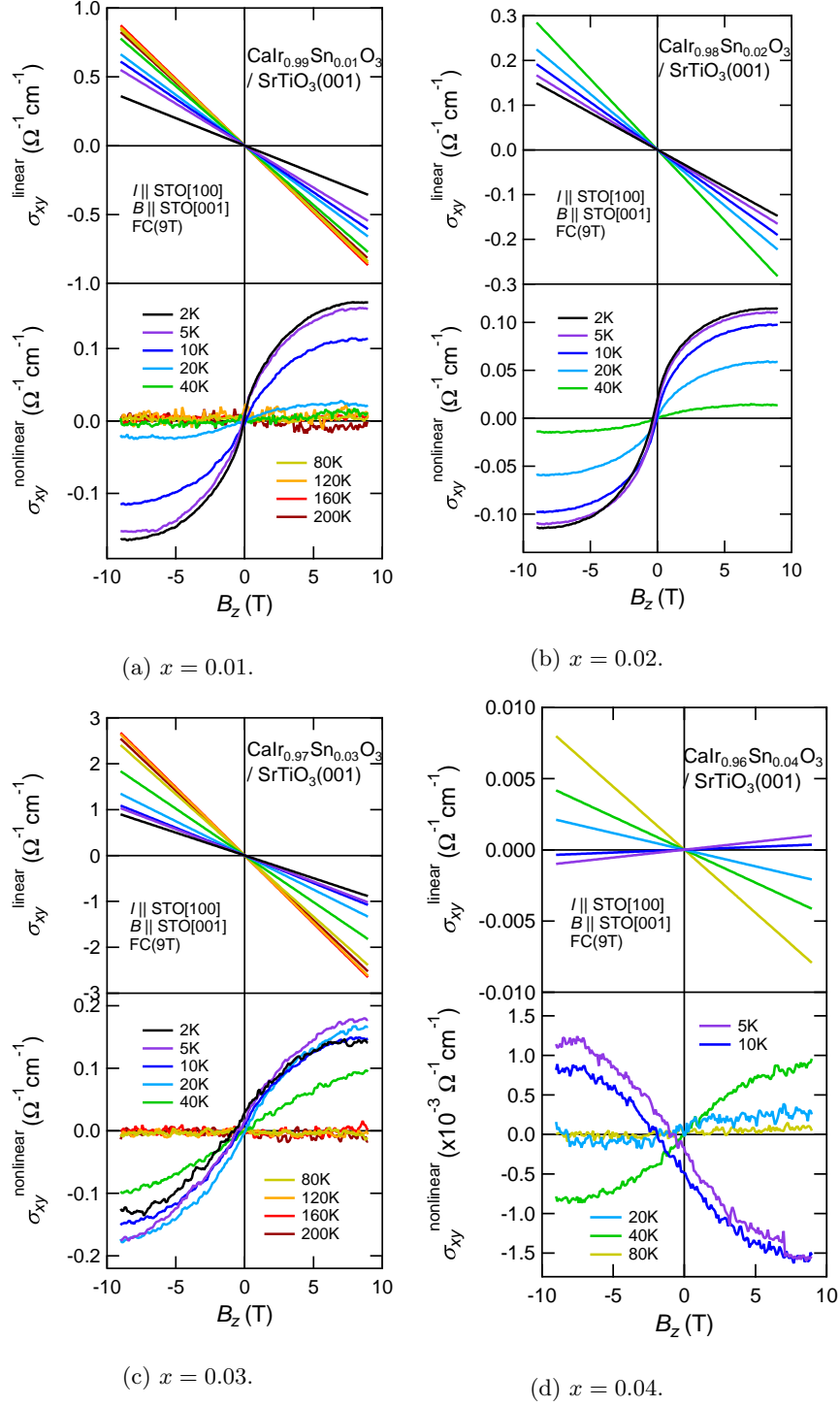


Figure 3.30: Linear and nonlinear parts of $\sigma_{yx}(B_z)$ of $\text{CaIr}_{1-x}\text{Sn}_x\text{O}_3$ films ($x = 0.01, 0.02, 0.03, 0.04$).

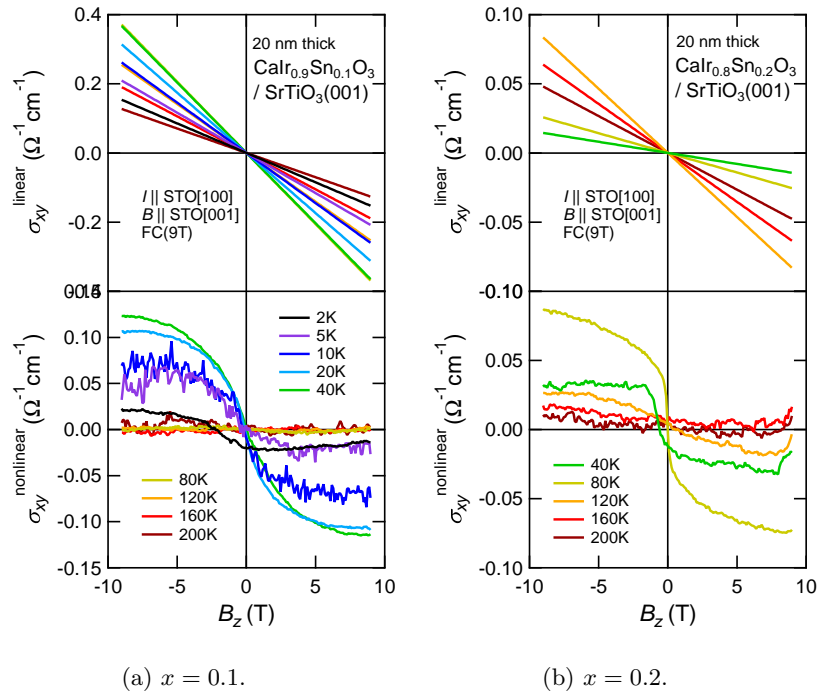


Figure 3.31: Linear and nonlinear parts of $\sigma_{yx}(B_z)$ of $\text{CaIr}_{1-x}\text{Sn}_x\text{O}_3$ films ($x = 0.1, 0.2$). These two samples are 20 nm-thick samples, since Hall measurements on 10 nm-thick samples with high resistivity were difficult.

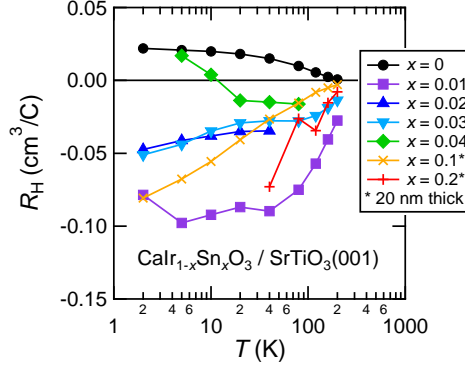


Figure 3.32: Hall coefficient of perovskite $\text{CaIr}_{1-x}\text{Sn}_x\text{O}_3$ / $\text{SrTiO}_3(001)$ films estimated from linear part of Hall resistivity $\sigma_{xy}(B_z)$

conductivity is observed for $0.04 \leq x \leq 0.2$. At $x = 0.04$, the S-shaped $\sigma_{xy}(B_z)$ is observed above 20 K, the Z-shaped $\sigma_{xy}(B_z)$ is observed below 10 K. We propose a hypothesis to explain these behaviors of Hall resistivity. Our hypothesis is that the S-shaped $\sigma_{xy}(B_z)$ comes from multi-carrier effects, and that the Z-shaped $\sigma_{xy}(B_z)$ comes from the anomalous Hall effect. This hypothesis will explain why the shape of $\sigma_{xy}(B_z)$ at $x = 0.04$ changes by temperature. Above 20 K, the Z-shaped anomalous Hall conductivity will not be so large compared to the usual S-shaped Hall effect, and the S-shaped $\sigma_{xy}(B_z)$ appears in the data. As temperature decreases, the weak ferro-magnetization will develop, and the Z-shaped anomalous Hall effect will become larger. The anomalous Hall effect will overcome the usual Hall effect below 10 K, which will result in the Z-shaped $\sigma_{xy}(B_z)$. Since hysteresis in $\sigma_{xy}(B_z)$ appears from $x \sim 0.02$, the anomalous Hall effect may appear from $x \lesssim 0.02$. To test this hypothesis, direct measurements of weak ferromagnetism including $M(B)$ data and determination of magnetic phase diagram are necessary.

Because we cannot conclude the origin of nonlinear Hall resistivity, precise estimation of carrier density based on Hall effect is difficult at the moment. However, the rough tendency about how Sn doping changes carrier balance can be obtained by looking at global change of the Hall behavior. Fig. 3.32 shows Hall coefficient of $\text{CaIr}_{1-x}\text{Sn}_x\text{O}_3$ films estimated from linear part of Hall resistivity $\sigma_{xy}(B_z)$. Of course these values are not accurate because the nonlinear part of $\sigma_{xy}(B_z)$ will probably contain nonlinearity caused by multi-carrier effects, but it will be useful to grab global tendency. According to Fig. 3.32, positive R_H at $x = 0$ turns negative by 1 % substitution, then more Sn substitution decreases $|R_H|$, and Hall behavior depends not so much on substitution ratio at large x region, though several inconsistent details like sign changing behavior at $x = 0.04$ exist. This rough tendency naïvely means that appearance and increase of electron-type carriers with relatively high mobility is caused by Sn doping. This tendency is similar to R_H of Sn-doped SrIrO_3 films, and therefore will be reasonable.

3.3.3 Discussion

We revealed that perovskite SrIrO_3 and CaIrO_3 take clearly distinct ways to reach insulating states under introduction of disorders. Especially, properties of $\text{CaIr}_{1-x}\text{Sn}_x\text{O}_3$ were at the first time realized and investigated by us. We argue that these contrasting Sn doping effects will reflect different scales of correlation in these semimetals.

The semimetal-to-insulator transition of SrIrO_3 is clearly triggered by the magnetism. Above the magnetic transition temperature, SrIrO_3 remains semimetallic resistivity even under 20% substitution of iridium which forms energy bands near the Fermi energy and provides conducting electrons. This stability of the semimetallic properties against introduction of disorders may be explained by large overlapping of Dirac electron band and other energy bands.

In contrast to SrIrO_3 , the insulating behavior of Sn doped CaIrO_3 enhanced by 1% doping of Sn suggests that disorders directly break the semimetallic conducting state and develops localization and insulating behavior. This sensitivity of the semimetallic properties against disorders may come from the electronic state where the Dirac node comes close to E_F by strong correlation, suggested by the study on bulk [14]. Large thickness-dependence of resistivity of the doped films also suggests that enhanced correlation will concern the insulating behavior. The change of the sign of R_H by Sn doping also supports the existence of the Dirac node near E_F . Hall resistivity shows nonlinear and hysteretic behavior, which suggests coexistence of multi-carrier nonlinearity and anomalous Hall effect. Further investigation of magnetic properties and magnetic phase diagram is necessary to understand Hall behavior.

At the same substitution ratio $x = 0.2$, SrIrO_3 has higher transition temperature and larger magnetization per iridium than CaIrO_3 . These differences support the above-mentioned interpretations about origins of the semimetal-insulator transitions, because SrIrO_3 will have larger stabilization energy of the magnetism by changing its electronic state concomitant with the magnetic transition.

For both $\text{Sr/CaIr}_{1-x}\text{Sn}_x\text{O}_3$, Sn substitution increases the number of electron-type carriers with relatively high mobility. This suggests that band deformation caused by Sn doping makes the energy level of the Dirac nodes lower. The shift of Hall effect of $\text{CaIr}_{1-x}\text{Sn}_x\text{O}_3$ from positive to negative also supports down shift of the nodal energy. We argue that these down shifts of the nodes are similar effects to the down shift of the node in pressured CaIrO_3 bulk [40]. Sn doping on Sr/CaIrO_3 increases bulk lattice constants while it does not change those of SrTiO_3 substrate, which means that Sn doping will enhance compressive strain on Sr/CaIrO_3 thin films whose in-plane lattices are fixed to SrTiO_3 substrate.

Is there any signature of topological properties of the Dirac line nodes? At the moment, we cannot say anything certain, but we can indicate two possibilities which may concern the topological properties of the Dirac line nodes. To test these hypotheses, further research is necessary.

For $\text{SrIr}_{1-x}\text{Sn}_x\text{O}_3$, the semimetal-insulator transition triggered by the magnetism may come from a gap opening of the Dirac node by symmetry breaking due to the magnetism. To test this hypothesis, one should check the existence of the Dirac electron pocket and confirm that the electron pocket starts to shrink around the temperature where the magnetism appears. For such investigation,

ARPES will be a powerful probe. Therefore, the first realization of the epitaxial thin films of Sn doped SrIrO_3 in our study will be one-step progress from polycrystalline bulk. One difficulty is that the magnetism appears in the highly doped region $x > 0.1$. It is not a trivial problem whether the picture for the Dirac node protected by the symmetry is still valid in such highly substituted systems.

For $\text{CaIr}_{1-x}\text{Sn}_x\text{O}_3$, there is a possibility that the anomalous Hall signal may reflect non-trivial Berry curvature for the Dirac nodes. However, it is known that scattering processes also cause anomalous Hall effect [10]. Since scattering due to disorders will be important for Sn-doped CaIrO_3 , we should carefully check possibilities of anomalous Hall effect with such extrinsic origins. In order to extract an anomalous Hall component from the Hall resistivity and to investigate origins of the anomalous Hall effect. In addition, it is unclear also in $\text{CaIr}_{1-x}\text{Sn}_x\text{O}_3$ whether the picture for the Dirac node protected by the symmetry is still valid in highly substituted systems.

3.4 Magnetism of Sn-doped perovskite iridates

3.4.1 Antiferromagnetism of Ir pseudo-spins

We investigated the details of magnetic order in the weak ferromagnetic phase of $\text{SrIr}_{1-x}\text{Sn}_x\text{O}_3$ using resonant X-ray scattering technique. We used $\text{SrIr}_{0.8}\text{Sn}_{0.2}\text{O}_3$ film grown on non-vicinal STO(001) substrate, containing both domains with crystalline orientation $c \parallel [100]$ and $[010]$ for the measurement. The weak ferromagnetic transition temperature of the sample is ~ 180 K.

Fig. 3.33 shows results of RXS diffraction at $(1/2, 1/2, 1/2)$ point in reciprocal space and X-ray absorption spectroscopy at the L_3 edge of Ir. RXS measured by $\sigma - \pi$ configuration shows a resonant peak, indicating magnetic order of Ir pseudo-spins of $J_{\text{eff}} = 1/2$ states. RXS magnetic diffraction peaks are observed at $(1/2, 1/2, n + 1/2)$ ($n = 1, 2, 3$) and $(0, 1/2, 1)$, and not observed in given SN ratio at $(1/2, 1/2, 1)$ or $(0, 0, 1/2)$. These results show that Ir pseudo-spins form G -type antiferromagnetic order, or NaCl-type order of pseudo-spins with opposite directions, at Ir sites.

Fig. 3.34 shows temperature-dependence of intensity of RXS magnetic diffraction at $(1/2, 1/2, 1/2)$. The diffraction appears below the weak ferromagnetic transition temperature. Therefore, the antiferromagnetic order observed by RXS is associated with weak ferromagnetism.

3.4.2 Magnetic anisotropy

Fig. 3.35 shows temperature-dependence of magnetization of $\text{SrIr}_{0.8}\text{Sn}_{0.2}\text{O}_3$ film for $[100]$, $[010]$ and $[001]$ directions. Weak ferromagnetic moment is observed below 200 K in case the field is parallel to the $[010]$ direction. In other cases where the field is along $[100]$ or $[001]$, the moment is too weak, and the transition is not clearly identified in the experimental data in the given SN ratio. The $[010]$ direction corresponds to the direction of step lines on STO substrate surface, and the c direction of orthorhombic unit cell of perovskite-type SrIrO_3 . Thus, the easy axis of magnetization in weak ferromagnetic phase is identified to the orthorhombic c axis of perovskite SrIrO_3 .

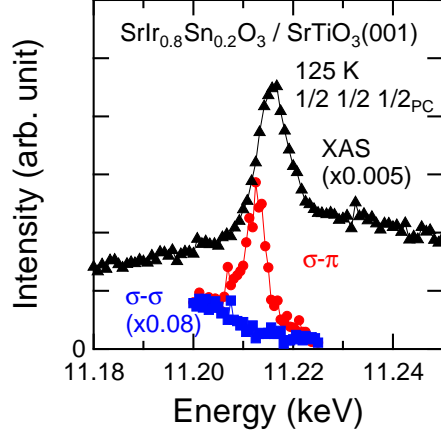


Figure 3.33: RXS diffraction at $(1/2, 1/2, 1/2)$ and XAS of perovskite $\text{SrIr}_{0.8}\text{Sn}_{0.2}\text{O}_3 / \text{SrTiO}_3(001)$ film.

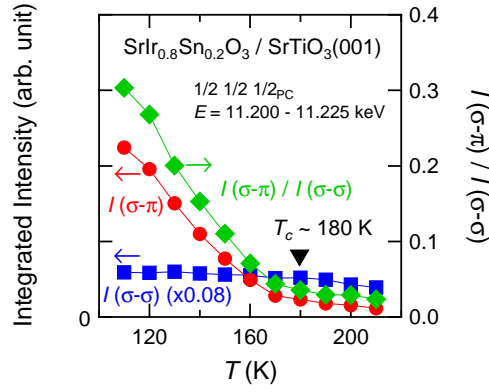


Figure 3.34: Temperature-dependence of intensity of RXS magnetic diffraction at $(1/2, 1/2, 1/2)$ of perovskite $\text{SrIr}_{0.8}\text{Sn}_{0.2}\text{O}_3 / \text{SrTiO}_3(001)$ film.

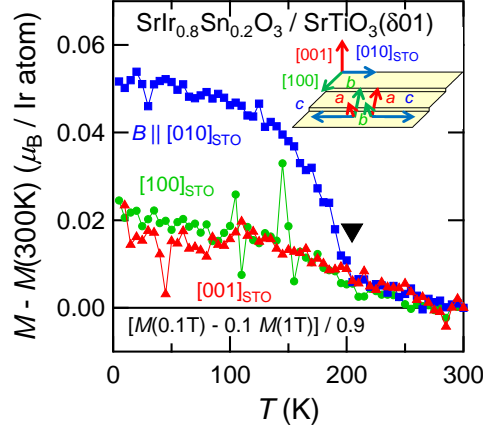


Figure 3.35: Temperature-dependent magnetization of perovskite $\text{SrIr}_{0.8}\text{Sn}_{0.2}\text{O}_3$ / $\text{SrTiO}_3(\delta 01)$ film under magnetic fields with different directions. The values in the graph are the total magnetization of the sample divided by the number of Ir atoms in the sample, not magnetization for each Ir ions.

For $\text{CaIr}_{1-x}\text{Sn}_x\text{O}_3$, weak ferromagnetic moment is observed when the field is parallel to $[001]$, as displayed in Fig. 3.24. The $[001]$ direction corresponds to the c direction of the orthorhombic unit cell of perovskite-type CaIrO_3 in the undoped system. As mentioned above, Sn doped CaIrO_3 / STO has all crystalline orientation $c \parallel [100]$, $[010]$ and $[001]$ though their existence ratio is unknown. A probable assumption is that domains with $c \parallel [001]$ stay as most of them even in doped systems. Under that assumption, the magnetic anisotropy of $\text{CaIr}_{1-x}\text{Sn}_x\text{O}_3$ / STO samples suggests that the easy axis of magnetization in the weak ferromagnetic phase will be the orthorhombic c axis. This statement agrees with SISO. Therefore, we conclude that the assumption above was reasonable.

3.4.3 Discussion

The results of RXS magnetic diffraction and anisotropy of magnetization enable discussion of detailed magnetic structure of Sn doped SrIrO_3 .

Since the antiferromagnetism of Ir pseudo-spins and the weak ferromagnetic moment appear at the same temperature, the weak ferromagnetic moment is attributed to canting of Ir pseudo-spins from ideal antiferromagnetic order. In iridates, strong spin-orbit coupling combines spin and orbital moments to $J_{\text{eff}} = 1/2$ pseudo-spins. Therefore, directions of each pseudo-spins will be affected by structural distortions of IrO_6 octahedra. In terms of effective interaction between two neighboring magnetic moments, spin orbit coupling and crystal structure without local inversion symmetry between the two moments causes an additional Dzyaloshinskii-Moriya (DM) interaction in addition to isotropic Heisenberg interaction. Though calculation of DM term from lattice information is difficult, symmetrical analysis of DM interaction and moment canting caused by DM interaction is easy by applying Moriya rules [47]. Consid-

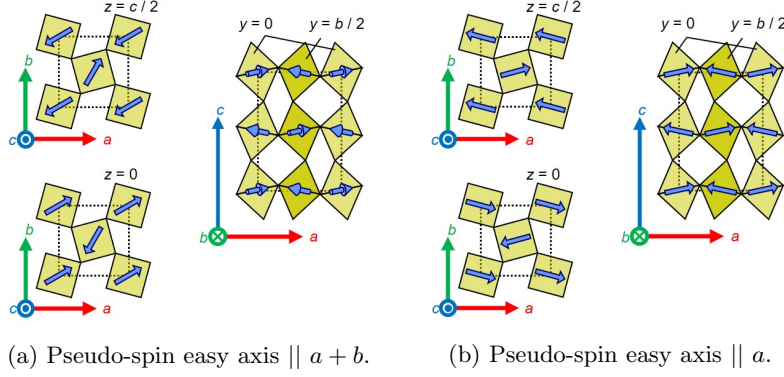


Figure 3.36: Schematic pictures of examples of possible magnetic structures of $\text{SrIr}_{1-x}\text{Sn}_x\text{O}_3$ films.

ering GdFeO_3 -type distorted orthorhombic perovskite ABO_3 with (pseudo)spins at each B sites and G -type antiferromagnetic order of them, the relationship between direction of each moments in un-distorted antiferromagnetic order and direction of weak ferromagnetic moment caused by canting is described as below.

1. In case each moment aligns along the a direction in un-distorted antiferromagnetism, moment canting will cause weak ferromagnetic moment along the c direction.
2. In case each moment aligns along the b direction in un-distorted antiferromagnetism, moment canting will cause no weak ferromagnetic moment.
3. In case each moment aligns along the c direction in un-distorted antiferromagnetism, moment canting will cause weak ferromagnetic moment along the a direction.

The experiments on $\text{Sr}/\text{CaIr}_{0.8}\text{Sn}_{0.2}\text{O}_3$ show that weak ferromagnetic moments appear along the c directions. Thus, Ir pseudo-spins in the antiferromagnetism should lie in the ab plane to satisfy the third condition, but they should not be parallel to the b axis to satisfy the first condition. They do not necessarily have to be parallel to the a direction (like Fig. 3.36b) in order to satisfy the first condition. For example, arrangements where pseudo-spin easy axis of the antiferromagnetism is parallel to the $a \pm b$ directions (such as Fig. 3.36a) are also allowed.

Considering symmetry of $J_{\text{eff}} = 1/2$ electronic state, Ir pseudo-spins will be more likely to lie along directions of Ir-O bonds than others. Therefore, Ir pseudo-spins in canted antiferromagnetism of $\text{Sr}/\text{CaIr}_{1-x}\text{Sn}_x\text{O}_3$ may also align along the $a \pm b$ directions. The more detailed magnetic structure is still an open question.

Chapter 4

Conclusion

Dirac electron systems and strongly correlated electron systems are both important fields in solid state research. Orthorhombic perovskite iridium oxides $A\text{IrO}_3$ ($A = \text{Sr}, \text{Ca}$) are the materials which are located near the boundary between these two fields. Their spin-orbit-entangled electronic states host the Dirac line node topologically protected by the nonsymmorphic crystalline symmetry. Proximity to magnetic insulators indicates that electron correlation also has an important role in these materials. In addition, effective strength of correlation in $A\text{IrO}_3$ can be controlled by changing A sites, and CaIrO_3 is supposed to have stronger correlation. For SrIrO_3 with weaker correlation, partial substitution of Ir sites by non-magnetic Sn ions reduces electron conduction among Ir sites, and relatively enhanced correlation causes transition from the Dirac semimetal to a magnetic insulator. In this context, how the more strongly correlated Dirac nodal state of CaIrO_3 reacts to Sn doping is an interesting problem, but has remained un-investigated before our work.

We synthesized Sn-doped CaIrO_3 at the first time, and compared it with the Sn substitution effect on SrIrO_3 . The results show that Sn doped CaIrO_3 reaches a magnetic insulator in a completely different way from that of SrIrO_3 . While Sn-doped SrIrO_3 shows the magnetism-triggered semimetal-insulator transition similarly to the previous report, Sn-doped CaIrO_3 develops insulating behavior independently of the magnetism. The insulating behavior of Sn-doped CaIrO_3 is probably assisted by both correlation and disorder effects, suggesting an interplay of correlation and disorders. This discovery of the contrasting Sn substitution effects on Sr/CaIrO_3 is the first example to show that different strengths of correlation result in a variety of quantum phases in $5d$ Dirac electron systems. Therefore, we believe that our study will inspire further research on perovskite Sr/CaIrO_3 , Dirac line node semimetals with controllable correlation.

On the other hand, the quest for topological properties of the symmetry-protected Dirac line nodes remains a future problem. We obtained some results which may have relation with topological properties of the nodes, like the anisotropic magnetoresistance of undoped SrIrO_3 and the anomalous Hall effect of Sn-doped CaIrO_3 , but at the moment we cannot state about those relations due to lack of reasonable interpretation or experimental evidence. Especially for the latter example, we hope that future investigation of magnetic properties and magnetic phase diagrams on Sn-doped CaIrO_3 will enable us to understand nonlinear Hall resistivity and origins of the anomalous Hall effect.

In conclusion, we revealed that interplays of electron correlation and disorders realize various ways of transitions from Dirac nodal semimetal to magnetic insulator corresponding strength of correlation, by investigating effects of elemental substitution in perovskite iridates, Dirac line node semimetal with controllable correlation. Our results demonstrate rich physics behind materials which are located near the phase boundary between topological Dirac materials and strongly correlated materials.

Chapter 5

Acknowledgements

The experimental results on orthorhombic perovskite $\text{Alr}_{1-x}\text{Sn}_x\text{O}_3$ films excluding the XPS and the RXS experiment have already been published as: Masamichi Negishi, Naoka Hiraoka, Daisuke Nishio-Hamane, and Hidenori Takagi, “Contrasted Sn substitution effects on Dirac line node semimetals SrIrO_3 and CaIrO_3 ” *APL Mater.* 7, 121101 (2019); <https://doi.org/10.1063/1.5129235>.

For research, I thank the collaborators in this work; Prof. Dr. Hidenori Takagi and Dr. Hiraoka Naoka for supervising the project, Dr. Kentaro Kitagawa for discussion, Mr. Naoki Matsui for help of synthesis and measurement of monoclinic SrIrO_3 , Dr. Daisuke Nishio-Hamane for the observation by transmission electron microscope, Prof. Dr. Takahisa Arima and Dr. Hiroyuki Ohsumi for the RXS measurement, Prof. Dr. Hiroshi Kumigashira, Prof. Dr. Koji Horiba, Dr. Miho Kitamura and Dr. Ryu Yukawa for the XPS measurement. I also thank Dr. Gennady Logvenov, Mr. Georg Cristiani, Dr. Graham McNally, Mr. Frank Falkenberg, Dr. Minu Kim, Dr. Yosuke Matsumoto, Mr. Mohammad Pakdaman, for collaboration and/or helps for other research projects in my Ph.D. course, though the scientific results are not mentioned in this paper.

I thank the committee members for this Ph.D. thesis, Prof. Dr. Satoru Nalatsuji, Prof. Dr. Naoto Tsuji, Prof. Dr. Yoshiya Uwatoko, Prof. Dr. Masashi Tokunaga, and Prof. Dr. Mikk Lippma for useful discussion and advice to improve this work.

For education, I thank Prof. Dr. Hidenori Takagi as supervisor, Dr. Kentaro Kitagawa and Dr. Hiraoka Naoka as daily education. I also thank Prof. Dr. Zenji Hiroi as sub-supervisor of MERIT (Materials Education program for the future leaders in Research, Industry, and Technology). I thank the secretaries in our research groups, Ms. Reiko Nagashima and Ms. Sabine Paulsen, for the official support. I thank all colleagues in the research groups, both in Tokyo and Stuttgart, for their kindness in daily activities.

I thank the above-mentioned MERIT and Japan Society for the Promotion of Science for financial support during my Ph.D. course.

Bibliography

- [1] W. Wu, Y. Liu, S. Li, C. Zhong, Z.-M. Yu, X.-L. Sheng, Y. X. Zhao, and S. A. Yang. *Phys. Rev. B*, 97:2115125, 2018.
- [2] X. Zhang, Z.-M. Yu, Z. Zhu, W. Wu, S.-S. Wang, X.-L. Sheng, and S. A. Yang. *Phys. Rev. B*, 97:235150, 2018.
- [3] N. P. Armitage, E. J. Mele, and A. Vishwanath. *Rev. Mod. Phys.*, 90:015001, 2018.
- [4] K. S. Novoselov, A. K. Geim, S. V. Morozov, D. Jiang, M. I. Katsnelson, I. V. Grigorieva, S. V. Dubonos, and A. A. Firsov. *Nature*, 438:197–200, 2005.
- [5] J. J. Yeh and I. Lindau. *Atomic Data and Nuclear Data Table*, 132:1–155, 1985.
- [6] Y. Cao, V. Fatemi, S. Fang, K. Watanabe, T. Taniguchi, E. Kaxiras, and P. Jarillo-Herrero. *Nature*, 556:43–50, 2018.
- [7] Y. Cao, V. Fatemi, A. Demir, S. Fang, S. L. Tomarken, J. Y. Luo, J. D. Sanchez-Yamagishi, K. Watanabe, T. Taniguchi, E. Kaxiras, R. C. Ashoori¹, and P. Jarillo-Herrero.
- [8] K. Kuroda, T. Tomita, M.-T. Suzuki, C. Bareille, A. A. Nugroho, P. Goswami, M. Ochi, M. Ikhlas, M. Nakayama, S. Akebi, R. Noguchi, R. Ishii, N. Inami, K. Ono, H. Kumigashira, A. Varykhalov, T. Muro, T. Koretsune, R. Arita, S. Shin, Takeshi Kondo, and S. Nakatsuji. *Nat. Mater.*, 16:1090–1095, 2017.
- [9] D. F. Liu, A. J. Liang, E. K. Liu, Q. N. Xu, Y. W. Li, C. Chen, D. Pei, W. J. Shi, S. K. Mo, P. Dudin, T. Kim, C. Cacho, G. Li, Y. Sun, L. X. Yang, Z. K. Liu, S. S. P. Parkin, C. Felser, and Y. L. Chen. *Science*, 365:1282–1285, 2019.
- [10] N. Nagaosa, J. Sinova, S. Onoda, A. H. MacDonald, and N. P. Ong. *Rev. Mod. Phys.*, 82:1539, 2010.
- [11] B. J. Kim, Hosub Jin, S. J. Moon, J.-Y. Kim, B.-G. Park, C. S. Leem, Jaeyun Yu, T. W. Noh, C. Kim, S.-J. Oh, J.-H. Park, V. Durairaj, G. Cao, and E. Rotenberg. *Phys. Rev. Lett.*, 101:076402, 2008.
- [12] B. J. Kim, H. Ohsumi, T. Komesu, S. Sakai, T. Morita, H. Takagi, and T. Arima. *Science*, 323:1329–1332, 2009.

- [13] J. M. Carter, V. V. Shankar, M. A. Zeb, and H.-Y. Kee. *Phys. Rev. B*, 85:115105, 2012.
- [14] J. Fujioka, R. Yamada, M. Kawamura, S. Sakai, M. Hirayama, R. Arita, T. Okawa, D. Hashizume, M. Hoshino, and Y. Tokura. *Nat. Comm.*, 10:362, 2019.
- [15] J. M. Longo, J. A. Kafalas, and R. J. Arnett. *J. Sol. Stat. Chem.*, 3:174–179, 1971.
- [16] C. L. McDaniel and S. J. Schneider. *J. Sol. Stat. Chem.*, 4:275–280, 1972.
- [17] Y. Chen, H.-S. Kim, and H.-Y. Kee. *Phys. Rev. B*, 93:155140, 2016.
- [18] K. Hirose and Y. Fujita. *Geophys. Res. Lett.*, 32:12, 2005.
- [19] Y. K. Kim, A. Sumi, K. Takahashi, S. Yokoyama, S. Ito, T. Watanabe, K. Akiyama, S. Kaneko, and H. Funakubo. *Jpn. J. Appl. Phys.*, 45:L36, 2006.
- [20] L. Zhang, B. Pang, Y. B. Chen, and Y. Chen. *Critical Reviews in Solid State and Materials Sciences*, 43:5:367–391, 2018.
- [21] S. Y. Jang, H. Kim, S. J. Moon, W. S. Choi, B. C. Jeon, J. Yu, and T. W. Noh. *J. Phys.: Condens. Matter*, 22:485602, 2010.
- [22] A. Biswas and Y. H. Jeong. *J. Appl. Phys.*, 117:195305, 2015.
- [23] D. Hirai, J. Matsuno, D. Nishio-Hamane, and H. Takagi. *Appl. Phys. Lett.*, 107:012104, 2015.
- [24] M. Masuko, J. Fujioka, M. Nakamura, M. Kawasaki, and Y. Tokura. *APL Mater.*, 7:081115, 2019.
- [25] B. L. Chamberland and A. R. Philpotts. *Journal of Alloys and Compounds*, 182:355–364, 1992.
- [26] R. D. Shannon. *Acta Cryst.*, A 32:751, 1976.
- [27] A. Vegas, M. Vallet-Regi, J. M. Gonzalez-Calbet, and M. A. Alario-Franco. *Acta Cryst.*, B42:167–172, 1986.
- [28] J. G. Zhao, L. X. Yang, Y. Yu, F. Y. Li, R. C. Yu, Z. Fang, L. C. Chen, and C. Q. Jin. *J. Appl. Phys.*, 103:103706, 2008.
- [29] P. E. Blanchard, E. Reynolds, B. J. Kennedy, J. A. Kimpton, M. Avdeev, and A. A. Belik. *Phys. Rev. B*, 89:214106, 2014.
- [30] J. Fujioka, T. Okawa, A. Yamamoto, and Y. Tokura. *Phys. Rev. B*, 95:121102(R), 2017.
- [31] A. A. Abrikosov. *Europhys. Lett.*, 49(6):789–793, 2000.
- [32] L. Zhang, H.-Y. Wu, J. Zhou, F.-X. Wu, Y. B. Chen, S.-H. Yao, S.-T. Zhang, and Y.-F. Chen. *Appl. Surf. Sci.*, 280:282–286, 2013.

- [33] J. Liu, D. Kriegner, L. Horak, D. Puggioni, C. Rayan Serrao, R. Chen, D. Yi, C. Frontera, V. Holy, A. Vishwanath, J. M. Rondinelli, X. Marti, and R. Ramesh. *Phys. Rev. B*, 93:085118, 2016.
- [34] L. Horák, D. Kriegner, J. Liu, C. Frontera, X. Marti, and V. Holý. *J. Appl. Cryst.*, 50:385–398, 2017.
- [35] Y. F. Nie, P. D. C. King, C. H. Kim, M. Uchida, H. I. Wei, B. D. Faeth, J. P. Ruf, J. P. C. Ruff, L. Xie, X. Pan, C. J. Fennie, D. G. Schlom, and K. M. Shen. *Phys. Rev. Lett.*, 114:016401, 2015.
- [36] Z. T. Liu, M. Y. Li, Q. F. Li, J. S. Liu, W. Li, H. F. Yang, Q. Yao, C. C. Fan, X. G. Wan, Z. Wang, and D. W. Shen. *Sci. Rep.*, 6:30309, 2016.
- [37] J. Matsuno, K. Ihara, S. Yamamura, H. Wadati, K. Ishii, V. V. Shankar, H.-Y. Kee, and H. Takagi. *Phys. Rev. Lett.*, 114:247209, 2015.
- [38] A. Biswas, K.-S. Kim, and Y. H. Jeong. *J. Appl. Phys.*, 116:213704, 2014.
- [39] A. K. Jaiswal, R. Schneider, R. Singh, and D. Fuchs. *Appl. Phys. Lett.*, 115:031904, 2019.
- [40] R. Yamada, J. Fujioka, M. Kawamura, S. Sakai, M. Hirayama, R. Arita, T. Okawa, D. Hashizume, M. Hoshino, and Y. Tokura. *Phys. Rev. Lett.*, 123:216601, 2019.
- [41] J.-G. Cheng, J.-S. Zhou, J. B. Goodenough, K. Matsubayashi, and Y. Uwatoko. *JPS Conf. Proc.*, 3:013014, 2014.
- [42] Q. Cui, J.-G. Cheng, W. Fan, A. E. Taylor, S. Calder, M. A. McGuire, J.-Q. Yan, D. Meyers, X. Li, Y. Q. Cai, Y. Y. Jiao, Y. Choi, D. Haskel, H. Gotou, Y. Uwatoko, J. Chankhalian, A. D. Christianson, S. Yunoki, J. B. Goodenough, and J.-S. Zhou. *Phys. Rev. Lett.*, 117:176603, 2016.
- [43] J. Fujioka, T. Okawa, M. Masuko, A. Yamamoto, and Y. Tokura. *J. Phys. Soc. Jpn*, 87:123706, 2018.
- [44] R. G. Chambers. *Proc. Phys. Soc. A*, 65:903, 1952.
- [45] M. Yabashi, T. Mochizuki, H. Yamazaki, S. Goto, H. Ohashi, K. Takeshita, T. Ohata, T. Matsushita, K. Tamasaku, Y. Tanaka, and T. Ishikawa. *Nuclear Instruments and Methods in Physics Research A*, 467-468:678–681, 2001.
- [46] S. Grenier and Y. Joly. *J. Phys.: Conference Series*, 519:012001, 2014.
- [47] T. Moriya. *Phys. Rev.*, 120:91–98, 1960.
- [48] I. Qasim, B. J. Kennedy, and M. Avdeev. *J. Mater. Chem. A*, 1:3127–3132, 2013.
- [49] T. Takayama, A. N. Yaresko, and H. Takagi. *J. Phys.: Condens. Matter*, 31:074001, 2018.
- [50] A. Sumi, Y. K. Kim, N. Oshima, K. Akiyama, K. Saito, and H. Funakubo. *Thin Solid Films*, 486:182–185, 2005.

Appendix A

Monoclinic SrIrO_3

A.1 Introduction

Monoclinic SrIrO_3 has a three dimensional network of IrO_6 octahedra connecting each other at corner or face (Fig. A.1). Ir atoms align in the ab plane like the triangular lattice. Such the layers stack along the c direction with six-fold periodicity. The structure is almost hexagonal but slightly distorted to monoclinic. This structure is called as 6H or 6M by taking the periodicity along the c direction and the symmetry. The space group of the structure is No. 15 ($C 1 2/c 1$). The lattice parameters are given as $a = 5.60401(29) \text{ \AA}$, $b = 9.6256(4) \text{ \AA}$, $c = 14.1834(7) \text{ \AA}$ and $\beta = 93.202(4)^\circ$ [48].

Band calculation predicts that monoclinic SrIrO_3 will have Dirac nodes at A and M points on the boundary of the Brillouin zone (Fig. A.2) [49].

Polycrystalline bulk of monoclinic SrIrO_3 is paramagnetic, and shows semimetallic resistivity [49]. These results are consistent with the band calculation.

For thin film, there is a study which reported realization of monoclinic SrIrO_3 as epitaxial thin films on $\text{SrTiO}_3(111)$ substrates [50]. However, to our knowledge, there is no previous report which investigated electric transport properties of monoclinic SrIrO_3 thin films.

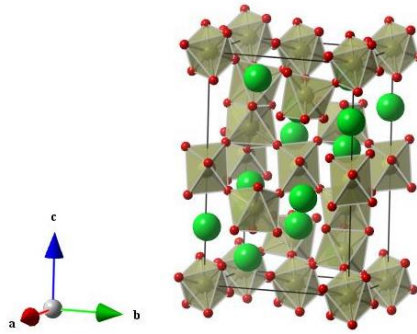


Figure A.1: Crystal structure of monoclinic SrIrO_3 [48]. Lime balls: Sr. Yellow balls: Ir. Red balls: O.

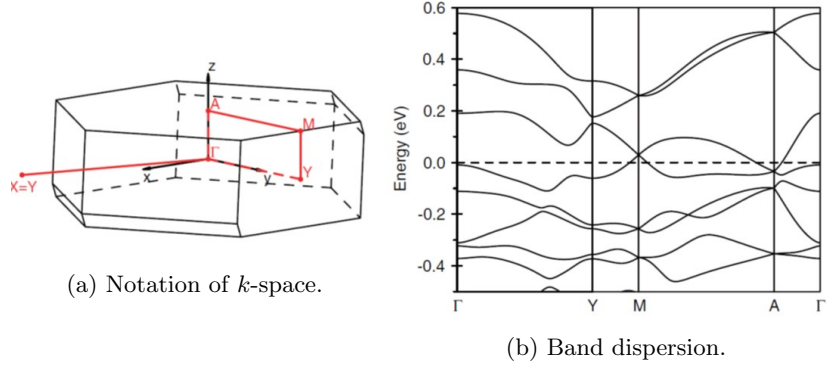


Figure A.2: LDA calculation of band structure of 6M SrIrO₃ with spin orbit coupling. The figures are quoted from T. Takayama *et al.* (2019) [49].

A.2 Methods

We synthesized epitaxial thin films of SrIrO₃ on SrTiO₃(111) substrates by pulsed laser deposition. We performed X-ray diffraction and X-ray reflectivity measurements for evaluation of crystal structure. We investigated transport properties of the samples. These methods are similar to those for perovskite iridates explained in the main article. For electric transport measurements of monoclinic SrIrO₃ / STO(111) samples, we used 5 mm \times 2.5 mm samples with edges parallel to $[2\bar{1}1]$ and $[01\bar{1}]$ directions and printed the single Hall bar pattern (Fig. 2.6a) on it. Thus, current is parallel to $[2\bar{1}1]$ or $[01\bar{1}]$, but not controlled¹.

A.3 Results

A.3.1 Crystal structure

Fig. A.3 shows a result of XRD 2θ - θ scan of a SrIrO₃ thin film sample fabricated on SrTiO₃(111) plane. Two sharp peaks at $2\theta = 40^\circ$ and 86° correspond to 111 and 222 reflections of the SrTiO₃ substrate. Peaks from the SrIrO₃ film show roughly three-fold periodicity of SrTiO₃ nnn reflections, which are identified as $0\ 0\ 2n$ reflections of the monoclinic phase of SrTiO₃. The out-of-plane lattice constant of the SrTiO₃ film is estimated as 14.17(1) Å and agrees with the bulk value ($c \sin(\beta) = 14.16$ Å [48]).

To investigate the epitaxial relationship between the film and the substrate, we conducted XRD reciprocal mapping around 231 and 131 SrTiO₃ diffraction spots (see Fig. A.4.). Film peaks around 231_{STO} are identified as $2\ 0\ 12$, $1\ 3\ 12$, $\bar{1}\ \bar{3}\ 12$ and $\bar{2}\ 0\ 12$, while ones around 131_{STO} are $2\ 2\ 11$, $0\ 4(\bar{4})\ 11$ and $\bar{2}\ \bar{2}\ 11$, though overlapping of the peaks makes it difficult to determine their precise positions. Therefore, relationship of crystalline orientation between film and substrate is summarized as below:

$$a \times b \parallel [111] \quad \text{and} \quad (\quad a \parallel [01\bar{1}] \quad \text{or} \quad a \parallel [\bar{1}01] \quad \text{or} \quad a \parallel [1\bar{1}0] \quad) \quad (\text{A.1})$$

¹We should have controlled it, but we did not notice inequivalence of $[2\bar{1}1]$ and $[01\bar{1}]$ when we did the experiments.

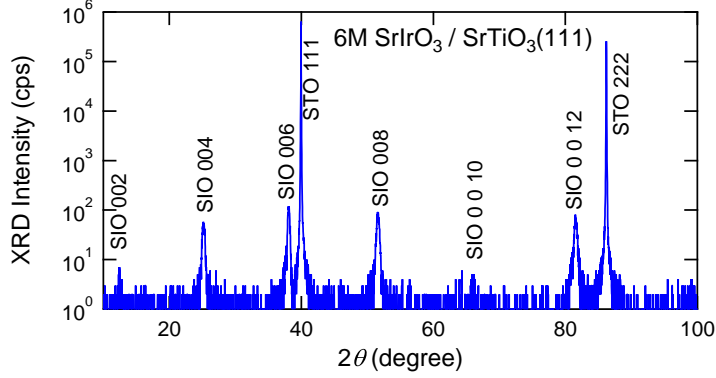


Figure A.3: XRD 2θ - θ scan of monoclinic (6M) SrIrO_3 / $\text{SrTiO}_3(111)$ film.

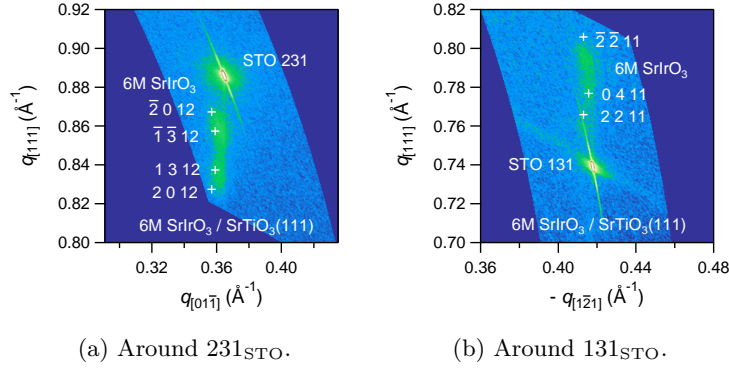


Figure A.4: XRD reciprocal space mapping of monoclinic (6M) SrIrO_3 / $\text{SrTiO}_3(111)$ film. Markers: calculated from bulk lattice constants.

The in-plane lattice of SrIrO_3 is not fixed to that of STO, but lattice parameters of film along $[01\bar{1}]_{\text{STO}}$ direction shrinks by $\sim 0.2 - 0.5 \%$ from bulk. Distances in reciprocal space between plus-minus pairs of diffractive points like $2\ 2\ 11_{\text{STO}}$ and $\bar{2}\ \bar{2}\ 11_{\text{STO}}$ shrink from estimation from bulk lattice constants, which suggests that the lattice constant β of SrIrO_3 becomes closer to 90° .

A.3.2 Semimetallic properties

Fig. A.5 shows experimental results of temperature-dependent resistivity of monoclinic SrIrO_3 thin films. Resistivity gradually decreases as temperature decreases, similarly to bulk [49]. This temperature-dependence supports the semimetallic electronic state.

Fig. A.6 displays measured Hall coefficients of monoclinic SrIrO_3 film samples. The results show V-shaped temperature-dependence and large sample-dependence. The temperature-dependence of R_H suggests existence of three kinds of conducting carriers: (1) hole-type carriers which has positive contribution on R_H at low temperature (< 10 K), (2) electron-type carriers which has negative contribution on R_H at moderate temperature (~ 50 K), and (3)

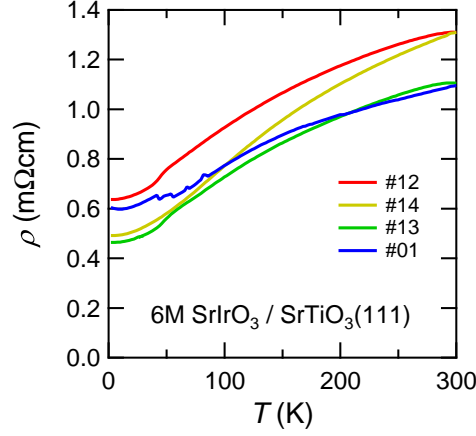


Figure A.5: Temperature-dependent resistivity of monoclinic (6M) SrIrO_3 / $\text{SrTiO}_3(111)$ films.

hole-type carriers which have positive contribution on R_H at high temperature (> 150 K). Since low temperature properties are determined by band structure very near the Fermi level E_F , (1) indicates a hole band crossing with the Fermi level. If several band crosses with the Fermi level, the one with highest mobility will be hole-type. On the other hand, (2) suggests that an electron band with higher mobility than hole (1) is located a few milli-electron volts above E_F . Therefore, (1) and (2) suggest the existence of Dirac nodes a few milli-electron volts above E_F . Positive Hall coefficient (3) comes from a non-Dirac hole band with large carrier density. Large sample-dependence of R_H indicates that carrier balance is strongly affected by sample quality, probably lattice relaxation or degree of oxygen deficiency.

Fig. A.7a shows magnetoresistance (MR) of monoclinic SrIrO_3 film and Fig. A.7b shows field direction-dependence of MR. MR takes its maximum value when the field is parallel to the current, indicating orbital contribution. MR is positive and linear-like. These features may be attributed to the linear MR at quantum limit which is often observed in semimetals with small Fermi surfaces [31], like Dirac semimetals.

A.4 Discussion

A.4.1 Crystal structure

As mentioned in the main article, AlIrO_3 hosts a variety of crystalline polytypes, and the monoclinic (6M) perovskite structure is a stable structure for bulk SrIrO_3 at ambient pressure. The orthorhombic perovskite phase is realized at high pressure and high temperature. In our experiments, SrIrO_3 grown on $\text{STO}(111)$ realizes the monoclinic phase, while SrIrO_3 on $\text{STO}(100)$ forms the perovskite phase. Reasons of the selective growth of the crystalline polytypes are attributed to characters of (001) and (111) planes, not strengths of epitaxial strain. We suggest two factors which will enable this selective growth.

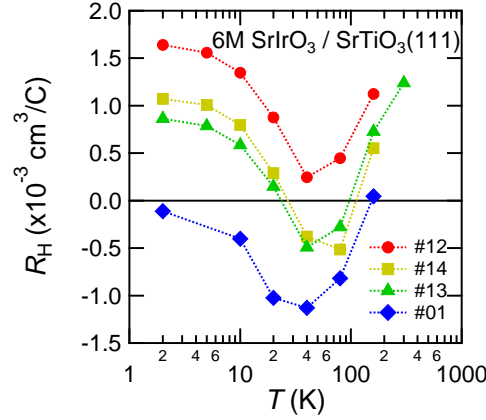
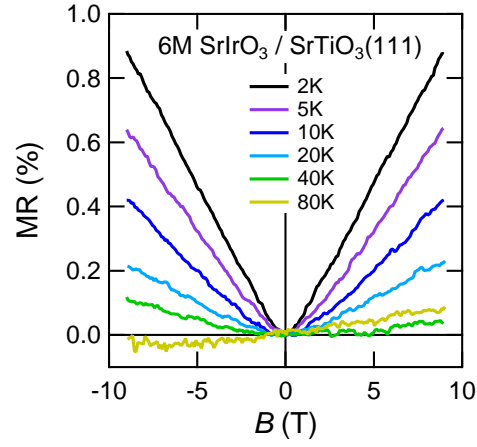


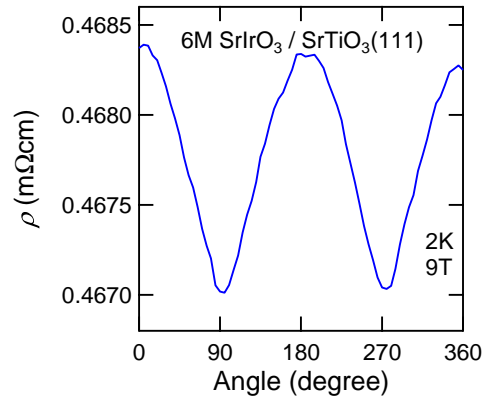
Figure A.6: Temperature-dependent Hall coefficient of monoclinic (6M) SrIrO_3 / $\text{SrTiO}_3(111)$ films.

- (1) **Similarity of crystal structures.** The orthorhombic perovskite structure of SrIrO_3 has only corner-sharing connections between IrO_6 octahedra and can be obtained by lattice distortions from cubic perovskite structure of SrTiO_3 . Therefore both (001) and (111) planes of SrTiO_3 will allow continuous connection to orthorhombic perovskite SrIrO_3 . On the other hand, the monoclinic SrIrO_3 has both corner- and face-sharing connections between IrO_6 octahedra. The direction of face-sharing connections is along the c axis of monoclinic SrIrO_3 unit cell, and IrO_6 octahedra align in the ab plane like the (111) plane in cubic perovskite. However, one cannot find a crystalline plane in monoclinic SrIrO_3 which has square-like periodicity like the (001) plane of cubic perovskite. This analysis supports the experimental results that the monoclinic SrIrO_3 phase grows not on (001)_{STO} but on (111)_{STO}.
- (2) **In-plane lattice fixing** The XRD results show that the in-plane lattice of perovskite SrIrO_3 is fixed to the substrate while that of monoclinic SrIrO_3 is partially relaxed. This means that perovskite SrIrO_3 on $\text{STO}(001)$ receives stronger compressive strain than monoclinic SrIrO_3 on $\text{STO}(111)$, which is consistent with the bulk phase diagram in which perovskite SrIrO_3 is located at high pressure. The reason for this difference of in-plane lattice fixing is still an open question.

We suggest a hypothesis that different charge ordering patterns of SrTiO_3 's surfaces may allow this difference of in-plane lattice fixing. When the [001] direction is defined as the stacking direction, the surface plane contains either $[\text{Sr}^{2+}\text{O}^{2-}]$ or $[\text{Ir}^{4+}(\text{O}^{2-})_2]$ ions. Therefore, the $\text{SrTiO}_3(001)$ plane has both positive and negative ions and will make a fluctuating potential for deposited particles. On the other hand, when the [111] direction is defined as the stacking direction the surface plane contains either $[\text{Sr}^{2+}(\text{O}^{2-})_3]$ or $[\text{Ir}^{4+}]$ ions. These planes are more homogeneous than (001) planes in terms of variation of the charges of the ions which the planes include. Therefore, the $\text{SrTiO}_3(111)$ plane will cause a more moderately changing potential



(a) Transverse magnetoresistance.



(b) Dependence of direction of external field. $B \parallel [111] \perp I$ for 0° . $B \parallel [1\bar{1}0] \parallel I$ for 90° .

Figure A.7: Magnetoresistance of monoclinic (6M) $\text{SrIrO}_3 / \text{SrTiO}_3(111)$ film.

on the surface than the $\text{SrTiO}_3(001)$ surface. This difference of the ordering patterns of charges in SrTiO_3 's surfaces may explain the difference of in-plane lattice fixing depending on (001) or (111) surfaces.

A.4.2 Semimetallic properties

Monoclinic SrIrO_3 films have large sample-dependency in Hall effect, which indicates semimetallic states with both electrons and holes. The scales of carrier density and mobility are roughly estimated as $n \sim +10^{21} \text{ cm}^{-3}$ and $\mu \sim +1 \text{ cm}^2\text{V}^{-1}\text{s}^{-1}$ using a single carrier model. Naïvely speaking, these values, relatively large carrier density and small mobility, have least “Dirac-ness” in the three materials investigated in this study. Probably the electrons and holes in this material, generated by the two distinct Dirac nodes, will have comparable densities and mobilities, and their cancellation may pretend small Hall coefficient $|R_H|$.

Appendix B

Data for Hall effect of Sn doped CaIrO_3

Fig. B.1 shows Hall resistivity of Sn doped CaIrO_3 films.

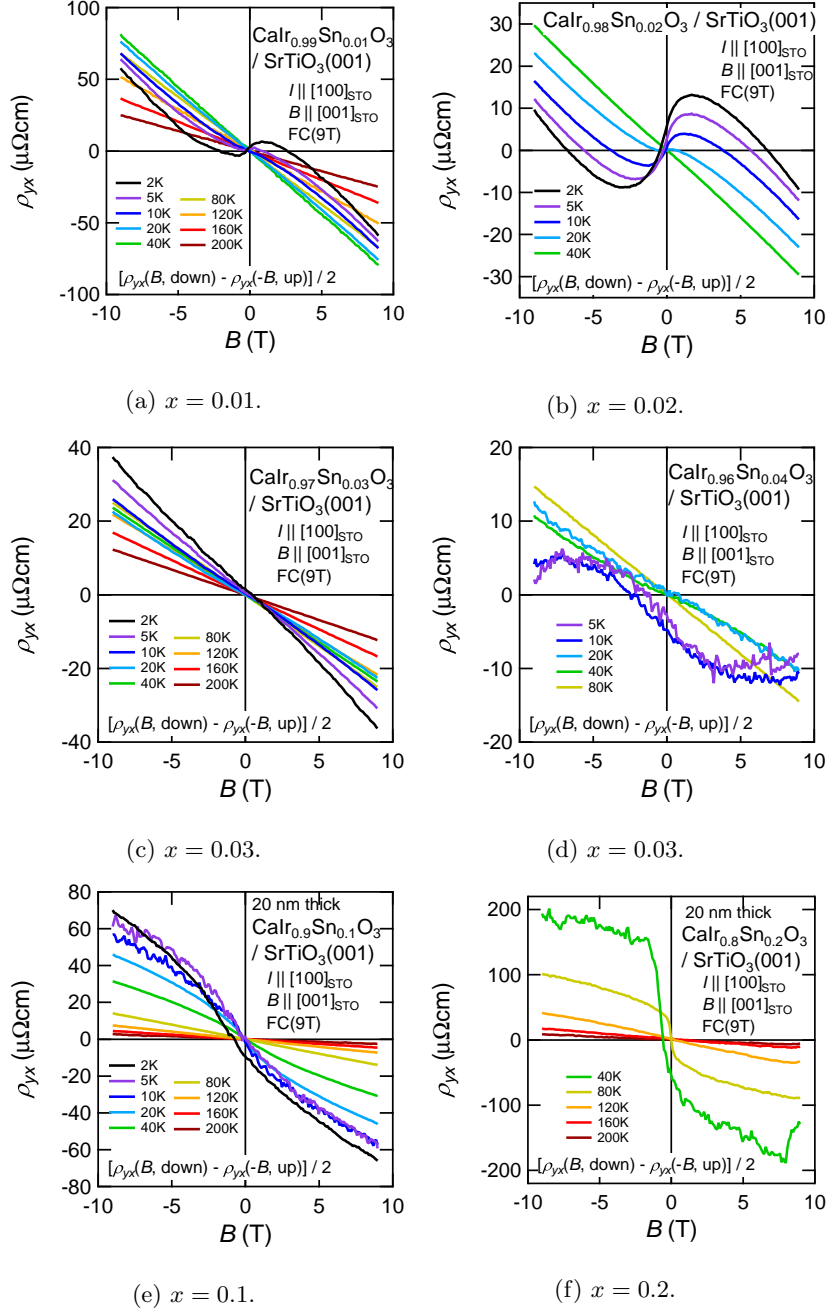


Figure B.1: Hall resistivity $\rho_{yx}(B_z)$ of $\text{CaIr}_{1-x}\text{Sn}_x\text{O}_3$ thin films. The samples for $x = 0.1$ and 0.2 are 20 nm-thick, since Hall measurements on 10 nm-thick samples with high resistivity were difficult.